Air-Ice-Ocean Coupling During a Strong Mid-Winter Cyclone, Part 1: Observing Coupled Dynamic Interactions Across Scales

D. M. Watkins[1], P. O. G. Persson[2], T. Stanton[3], A. Solomon[2], J. K. Hutchings[4] J. Haapala[5], G. Svensson[6]

[1]Center for Fluid Mechanics, Brown University, Providence, RI, USA. [2]Cooperative Institute for Research in Environmental Sciences, University of Colorado, Boulder CO and NOAA/Physical Sciences Laboratory, Boulder CO, USA. [3]Moss Landing Marine Laboratories and Naval Postgraduate School, CA, USA. [4]College of Earth Ocean and Atmospheric Sciences, Oregon State University, Corvallis, OR, USA. [5]Finnish Meteorological Institute, Helsinki, Finland. [6]Stockholm University, Stockholm, Sweden

Corresponding author: Daniel Watkins (daniel_watkins@brown.edu)

Key Points:

- A pair of cyclones crossed the Multidisciplinary drifting Observatory for the Study of the Arctic Climate (MOSAiC) in midwinter 2020
- Detailed, multi-platform observations enable characterization of coupled air-ice-ocean interactions during the passage of these cyclones
- The development of a low-level atmospheric jet is a key factor in the spatially and temporally varying sea ice-ocean response to cyclones

Abstract

Arctic cyclones are key drivers of sea ice and ocean variability. During the 2019-2020 Multidisciplinary drifting Observatory for the Study of Arctic Climate (MOSAiC) expedition, joint observations of the coupled air-ice-ocean system were collected at multiple spatial scales. Here, we present observations of a pair of strong mid-winter cyclones that impacted the MOSAiC site as it drifted in the central Arctic pack ice, with analytic emphasis on the second cyclone. The sea ice dynamical response showed spatial structure at the scale of the evolving atmospheric wind field. Internal ice stress and the ocean stress play significant roles, resulting in timing offsets between the atmospheric forcing and the ice response and post-cyclone inertial ringing in the ice and ocean. A structured response of sea ice motion and deformation to cyclone passage is seen, and the consequent ice motion then forces the upper ocean currents through frictional drag. The strongest impacts to the sea ice and ocean from the passing cyclone occur as a result of the surface impacts of a strong atmospheric low-level jet (LLJ) behind the trailing cold front. Impacts of the cyclone are prolonged through the coupled ice-ocean inertial response. The local impacts of the approximately 120 km wide LLJ occur over a 12 hour period or less and at scales of a kilometer to a few tens of kilometers, meaning that these impacts occur at smaller spatial scales and faster time scales than many satellite observations and coupled Earth system models can resolve.

Plain Language Summary

Arctic winter cyclones are an important part of the Arctic climate system. Yet, due to sparse observations, processes of the coupled sea ice-ocean response to cyclones are not fully understood. During the 2019-2020 Multidisciplinary drifting Observatory for the Study of Arctic Climate (MOSAiC) expedition, observations of the atmosphere, sea ice, and ocean were collected at a range of spatial scales. Here, we describe the atmospheric structure and coupled ice-ocean response to a strong winter cyclone using data from surface weather stations, weather balloons, radar, and a weather model. We then describe the sea ice motion using a large set of GPS buoys and ice radar images. Finally, we examine the upper ocean currents and structure using ocean buoy data. The most important part of the storm structure for the sea ice is the development of an atmospheric low-level jet (LLJ), a narrow region of fast-moving air that eventually circles around the storm. The sudden change in ice drift speed at the time that the LLJ

passes overhead enhances motion of the ice and ocean. Periodic currents in the ocean initiated by the sudden wind change of the LLJ continue for days following the passage of the storm, prolonging its effects.

1 Introduction

The physical environment in the Central Arctic consists of dynamically and thermodynamically coupled processes between the atmosphere, ice, and upper ocean (Brenner et al., 2023; Deser et al., 2015; Persson et al., 2017; Petty et al., 2016; Webster et al., 2019). Sea ice, and its accompanying snow cover, regulates the linkage between atmosphere and ocean through dynamics (lead opening and closing, evolving roughness of the air-ice and ice-ocean interfaces) and through thermodynamics as the ice and snow packs grow and melt (Maykut, 1982; Overland, 1985; Persson, 2002, 2012; Pinto et al., 2003; Ruffieux et al., 1995; von Albedyll et al., 2022). In turn, the stability of the atmospheric and ocean boundary layers governs the evolution of turbulent eddies, affecting the magnitude of turbulent fluxes of heat and momentum (Andreas et al., 2010a, b; Grachev et al., 2007; Lüpkes et al., 2008; Lüpkes & Gryanik, 2015; Taylor et al., 2018).

Arctic cyclones play a large role in this air-ice-ocean turbulent exchange. The large-scale pressure and mass fields of a cyclone produce strong winds near the central low and in air-mass transport belts along fronts. Therefore, cyclone passage results in a pulse of momentum, heat, and moisture into the ice-ocean system. They represent major sources of poleward heat and moisture transport during Arctic winter (Fearon et al., 2021) and impact the surface energy budget, ice growth, and even spring melt onset(Persson, 2012; Persson et al., 2017). Cyclone passage is often accompanied by strong sea ice deformation (Itkin et al., 2017; Lindsay, 2002; Oikkonen et al., 2017) and enhanced ocean mixing (Meyer et al., 2017a, b). Cyclone impacts on sea ice depend on time of year, cyclone strength and evolutionary stage, location within the Arctic, location relative to the ice edge and coast, and the sea ice state (Aue et al., 2022).

The direct dynamic impacts of cyclones on the sea ice momentum equation, expressed in Equation 1 (e.g., Hibler, 1979; Hunke et al., 2015) are transferred through the atmospheric stress term, $\boldsymbol{\tau_a}$:

$$m\,\frac{D\boldsymbol{u}}{Dt} = -mf\boldsymbol{k}\times\boldsymbol{u} + \boldsymbol{\tau_a} + \boldsymbol{\tau_o} - mg\,\nabla H + \nabla\cdot\boldsymbol{\sigma} \quad (1)$$

The left side of (1) is the rate of change of the ice momentum with approximately constant mass m (snow and sea ice mass per unit area), where $\boldsymbol{u}$ is the sea ice velocity. The sum of forces on the right-hand-side terms consists of the stresses on the ice due to the Coriolis force, where f is the Coriolis parameter, the atmosphere and ocean stress vectors $\boldsymbol{\tau_a}$ and $\boldsymbol{\tau_o}$, the effect of gravity down the slope of the ocean surface, and the divergence of the internal stress tensor. The last term represents energy loss due to friction between the floes and conversion of kinetic energy to potential energy, parameterized in terms of bulk and shear viscosities and ice strength. The coupled inertial response following the storm passage can prolong its dynamic effects (Haller et al., 2014).

The structure of the wind field within a cyclone imparts spatial gradients in the surface stresses, resulting in gradients of ice acceleration. As a result, the thermodynamic and dynamic sea ice response varies relative to the position of the low pressure center and the orientation of the storm track (e.g., Brümmer, 2003; Haapala et al., 2005; Kriegsmann & Brümmer, 2014; Overland & Pease, 1982). Composite analysis based on reanalysis and satellite observations demonstrate that sea ice impacts have spatial structure, with dependence on distance from the storm center (Kriegsmann & Brümmer, 2014) and position relative to the storm track (Clancy et al., 2022). However, estimates of cyclone structure and impacts based on composite analysis are sensitive to choices made in cyclone identification (Rae et al., 2017) and to the choice of reanalysis (Vessey et al., 2020). Differences in cyclone properties between reanalysis composites can arise from uncertainty in the physics of Arctic cyclones, differences in model implementation (including choice of parametrization schemes and model resolution), and the limited long-term in situ observations in the central Arctic, particularly joint observations of atmosphere, sea ice, and ocean.

Observations of the coupled air-ice-ocean system with the ability to resolve mesoscale cyclone features, including fronts, are extremely rare.Thermodynamic air-ice-ocean interactions for cyclones sampled during the Surface Heat and Energy Budget of the Arctic expedition (SHEBA; Persson, 2002; Uttal et al., 2002) have been analyzed at least in part in numerous studies (e.g., Lindsay, 2002; Persson, 2012; Persson et al., 2017; Richter-Menge et al., 2001; Shaw et al., 2009), providing case studies and seasonal and annual analysis. Both Lindsay (2002) and Richter-Menge et al., (2001) identify periods of enhanced mid-winter sea ice deformation that coincided with significant cyclone activity; however, the sea ice deformation observations lack sufficient resolution to examine air-ice dynamic coupling in detail. Measurements of sea ice motion and deformation show patterns related to the storm structure (Brümmer et al., 2008; Haller et al., 2014), with ice tending to diverge on average as the cyclone passes. The location of the ice edge and the local history of deformation is an important factor (Oikkonen et al., 2017).

The ocean response to wind forcing is strongly modulated by seasonal changes in ice thickness, roughness, and concentration (Gallaher et al., 2016; McPhee, 2002, 2008; Meyer et al., 2017a; Shaw et al., 2009; Stanton et al., 2012; Yang, 2004). Cyclones, and the strong gradients in winds associated with them, result in changes in momentum transfer to the ocean that can excite inertial oscillations in the ocean and ice (Brümmer & Hoeber, 1999; Hunkins, 1967), where the ice and ocean move together in an inertial ringing (Toole et al., 2010). The presence of ice can damp the ocean response (Brenner et al., 2023; Rainville & Woodgate, 2009), however inertial oscillations are observed in all seasons, including under consolidated winter ice pack (Martini et al., 2014). This momentum transfer and the inertial motion enhances mixing in the upper ocean and may also excite internal waves that enhance deeper mixing (McPhee & Kantha, 1989). High wind speeds over sea ice have been observed to produce increased ocean friction velocity (Shaw et al., 2009) and enhanced turbulent dissipation in the upper ocean (Meyer et al., 2017a). The winter ice cover impedes momentum transfer from the wind to the ocean, reduces the inertial response of the ocean, and likely sets the shallow winter mixed layer depth in parts of the Arctic Ocean (Toole et al., 2010). Buoy observations of sea ice drift suggest that the inertial response of the ice has been increasing (Gimbert et al., 2012; Yuan et al., 2022). It has been hypothesized that an increase in sea ice inertial response may arise due to thinning of the ice pack (Gimbert et al., 2012; Kwok et al., 2013) as well as increased cyclonic activity (Roberts et al., 2015).

To date, the full momentum transfer from wind, through ice to the ocean has not been observed directly on the temporal and spatial scales that clearly define the roles of the spatial structure of a cyclone for the associated ice and ocean response. To that end, we consider the detailed observations of the coupled-air-ice-ocean system obtained during the Multidisciplinary drifting Observatory for the Study of Arctic Climate (MOSAiC) expedition (Shupe et al., 2020; Shupe & Rex, 2022). This study examines the relative roles of the atmospheric stress, ocean stress (shearing between ice motion and upper-ocean currents), and the internal ice stress (via consideration of sea ice deformation) in the momentum balance from MOSAiC observations during the passage of two atmospheric cyclones that traversed the study area between 30 January and 2 February, 2020. While there were numerous cyclones during the MOSAiC year (Rinke et al., 2021), these two cyclones (especially the second cyclone) are of particular interest. They were intense, with high wind speed and low minimum sea level pressure. The sea ice response included the fastest winter drift speeds in the MOSAiC drift and strong deformation of the ice pack. The proximity of the storm track to the MOSAiC observatory allowed detailed observations of the cyclone development and ice-ocean response. Furthermore, the cyclones occurred during the consolidated ice season in the high Arctic, when the internal ice stress term is expected to be an important part of the response.

The study highlights the atmospheric features producing the atmospheric stress characteristics, and the impacts of these stress terms on the sea ice and ocean motion. While the atmospheric stress is generally regarded as the primary forcing mechanism for ice motion, it is shown that both the internal ice stress and the ocean stress play significant roles in changing the typical air-ice interaction characteristics, including producing timing offsets between the atmospheric forcing and the ice response and producing post-cyclone inertial "ringing" responses in the ice and ocean. The MOSAiC observations and additional data are described in section 2. Sections 3-5 describe the observations of atmosphere, sea ice, and ocean, respectively. Discussion and conclusions follow in Section 6.

2 Data and methods

The MOSAiC Central Observatory (CO) and its surrounding distributed network (DN) of automated observational platforms and buoys were deployed in residual ice north of the Laptev Sea in early October 2019, and drifted across the Central Arctic during the subsequent winter, entering the Fram Strait in June 2020 (Krumpen et al., 2020). Maps showing the track of the drifting station and more details of the atmospheric, ice, ocean and DN observations along this drift track can be found in a series of MOSAiC overview (Nicolaus et al., 2022; Rabe et al., 2022, 2024; Shupe et al., 2022) and domain-specific (e.g., Fer et al., 2022; Krumpen et al., 2021; Peng et al., 2023; von Albedyll et al., 2022; Watkins et al., 2023) publications. Figure 1 shows a map of the relative positions of the CO and the DN sites on Jan 31, 2020, at which time the CO was located at 87.5° N, 96.0° E (275 km from the North Pole).

2.1 Atmospheric observations

Atmospheric observations used in this study were made at the CO (both on board the *R/V Polarstern*, and at the "Met City" site located on the ice approximately 400 m from the ship), and at the three "L" sites located 10-25 km from the ship (Figure 1). Key measurements from the *R/V Polarstern* include the 6-hourly rawinsondes providing profiles of temperature, humidity, and horizontal winds, and the vertically-pointing Ka-band radar providing profiles of radar reflectivity and radial velocity. The 30-s radar data profiles were averaged to 10-min time intervals for this study. A DOE/ARM scanning Ka-band radar provided volumes of radar reflectivity and radial velocity approximately every 12 minutes, providing data for plane-parallel indicator (PPI) displays characterizing clouds and precipitation. Post-field program reflectivity calibrations were applied. Analyses of fronts and mesoscale features in the time-height cross sections and horizontal displays relied on standard subjective analyses of thermodynamic (e.g., temperature, virtual potential temperature (θ_v), equivalent potential temperature (θ_e)), kinematic (e.g., wind speed and direction), and radar reflectivity observations, not all of which are shown. Changes in θ_e and wind direction and minima in SLP were key markers for determining frontal boundaries. The Arctic inversion (AI) was defined as the height of the maximum temperature in each sounding, and varied distinctly as synoptic conditions changed. Surface-based layers of constant θ_v defined the surface mixed-layer (SML) depth for each sounding.

Sonic anemometers and basic meteorology sensors at Met City provided time series of temperature, humidity, winds, mean sea level pressure (SLP), and turbulence (including momentum flux) at 3 different levels (nominally 2, 6, and 10 m) and 4-component broadband radiative fluxes at ~2.5 m height. Atmospheric Surface Flux Stations (ASFS) located at the three L-sites provided measurements of temperature, humidity, pressure, and 4-component broadband radiative fluxes at ~2 m above the sea ice, and winds and turbulence (including momentum flux) at 3.8 m above the ice. The ASFS and Met City data used in this study are 10 minute average values. Unless otherwise stated, the Met City wind and turbulence data shown represents the 10 m height while those at the ASFS represent the 3.8 m height.

Atmospheric stress was obtained through covariance calculations using the 10 Hz three-component (u, v, w) measurements from the sonic anemometers at Met City and the ASFS. First, the earth coordinate system is rotated into streamwise coordinates through a double rotation

(Kaimal and Finnigan, 1994). The 10-min values of friction velocity $u_a^* = (u_s'w')^{1/2}$ were then obtained from the integration of the cross-spectral density for a 13.65 minute window centered on the 10 minute period. Here, u_s' and w' are perturbation values of the streamwise and vertical wind speeds, respectively. The observed atmospheric stress is then calculated by $\tau_a = \rho_a {u_a^*}^2$, where ρ_a is the atmospheric density. More detailed descriptions of the data processing, turbulence calculations and the atmospheric measurements on the *R/V Polarstern*, at Met City, and at the ASFS sites are provided by Shupe et al. (2022) and Cox et al. (2023).

Time series of low-level atmospheric divergence are calculated from the winds at the three L-sites using the assumption that the winds vary linearly between the three sites. With this assumption, the area-averaged low-level atmospheric divergence $\mathrm{div_a}$ can be calculated using the area-normalized divergence theorem and by integrating the winds normal to the sides of the polygon such that

$$\mathrm{div_a} \approx \frac{1}{A}\left[\sum_{i=1}^{n_s}\left(\bar{u}_i\,dy_i - \bar{v}_i\,dx_i\right)\right] \qquad (2)$$

where $n_s = 3$ is the number of sides, $\overline{u_i}, \overline{v_i}$ are the mean u and v wind components on side i, and $(\mathrm{dx_i}, \mathrm{dy_i})$ are the component lengths of each side i, and A is the area of the polygon. Because this calculation is sensitive to errors in the installation and manual orientation of the sonic anemometers, we assume that the long-term mean divergence between ASFS sensor alignments is zero, and subtract this mean value from each value in the time series. For this case, the long-

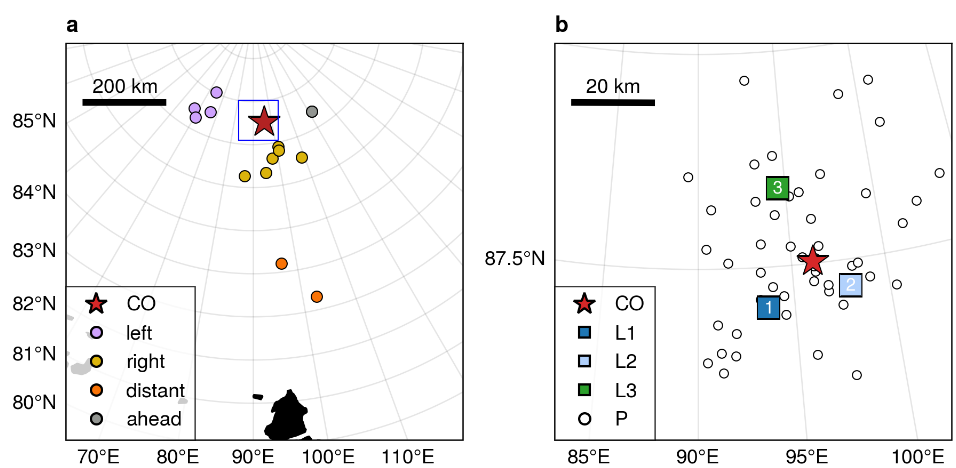

term mean divergence was $-1.1 \times 10^{-5}\mathrm{s}^{-1}$ calculated between 30 November, 2019, and 5 February, 2020. Hence, magnitudes of $\mathrm{div_a}$ larger than $2 \times 10^{-5}\mathrm{s}^{-1}$ are likely significant.

Figure 1. MOSAiC domain and instrument locations on 1 February 2020 at 00:00 UTC. Shown are a) the extended DN and b) the DN, defined as buoys within 60 km of the CO. The extent of panel b is shown by the open blue square in panel a. The Central Observatory (red star labeled CO) and the 3 "L-sites" with the ASFS, SIMB and AOFB (squares, right hand panel) measure complete atmospheric, ice and upper-ocean parameters. The GPS ice buoys (circles) measure position, and their colors in panel a correspond to groups defined and highlighted in Figures 7 and 9.

2.2 ERA5 atmospheric reanalysis

To obtain additional spatial atmospheric information, we supplement the atmospheric observations with 0.25° resolution data from the fifth-generation European Center for Medium-range Weather Forecasting reanalysis (ERA5; Hersbach et al., 2020) obtained from the Copernicus Data Store (Hersbach et al., 2023b, 2023a). Prior to analysis, the data was reprojected on a regular 25 km north polar stereographic grid with central longitude of 90°. The ERA5 reanalysis performs well relative to other reanalyses in the Arctic domain (Graham et al., 2019a, b). ERA5 is known to have a surface warm bias in the Arctic (C. Wang et al., 2019; Yu et al., 2021), and ERA5 low-level jets are slightly weaker and slightly elevated (López-García et al., 2022). Here, we use ERA5 mean sea level pressure, 10-m winds, and 925 hPa temperature and humidity, and 950 hPa winds. Rawinsonde and surface observations from the MOSAiC central observatory were assimilated by ERA5, as were surface measurements of temperature and air pressure from a few buoys from the MOSAiC DN. The ERA5 4D-var assimilation method uses a centered 12-h window, allowing impacts of observations to spread spatially and temporally. Hence, the ERA5 atmospheric structure should well represent the true atmospheric structure near the CO (as demonstrated for LLJs by López-García et al., 2022) and likely is the best available estimate of storm structure further away from the CO.

2.3 Sea ice observations

An array of drifting buoys, comprising the DN, track sea ice motion in the vicinity of the CO. Figure 1b shows the positions of the DN sites on February 1st, 2020 within 60 km of the central observatory. An additional 13 buoys comprise the "extended DN" (ExDN) and provide information on larger-scale ice motion (Figure 1a, colored circles). Each buoy reports positions via the Global Positioning System (GPS) with time resolution ranging from 10 minutes to 4 hours; the majority of buoys sampled at least once every hour. We only use buoys with (a) time resolution of three hours or less and (b) at least 80% data coverage between 25 January and 5 February 2020. Initial buoy processing is described in Bliss et al. (2023). In addition, anomalous points due to large random GPS errors were identified and removed by calculating the Z-score of the minimum of velocities estimated by forward and backward differences relative to a 3 day centered window. Observations were aligned to a 30 minute grid using natural cubic spline interpolation. During the study period, 64 buoys were operating, out of which 57 fulfill study criteria. These sites are referred to as position sites, or "P-sites". An additional 11 sites (including the L-sites and the CO) contain multiple instruments. We selected a reference buoy from each of these sites, preferring those with higher sampling rate and data precision (Table S1). Choice of reference buoys is arbitrary in most cases, as the buoys at each site are closely situated.

The buoy trajectories provide information about the divergence, shear and vorticity of sea ice inside the DN. We calculate strain-rate components using a Green's Theorem method, following Hutchings et al., (2012, errata 2018). The area over which deformation is estimated can be varied depending on sites chosen to surround the region of interest. We consider deformation on a variety of scales including: the triangle with L-sites at its vertices, a set of 5 polygons with length scales of 15-30 km covering the DN, a polygon enclosing the full DN with length scale 57 km (Figure 10), and two polygons for the left and right sections of the ExDN (Figure 9). Hence, the DN Full array is an estimate of average deformation within the DN, while the smaller polygons in Figure 10 give an indication of the variability within the array.

2.4 Sea ice radar imaging

Local sea ice deformation observations were obtained from a ship radar-image digitizing system. The system was connected to the 9.4 GHz X-band radar mounted at the roof of the *R/V*

Polarstern (Hessner et al., 2019). Images of sea ice backscatter were collected with 8.3 m resolution every 2.5 seconds. We use a set of processed and georeferenced images (Krumpen et al., 2021a) downsampled to approximately 15 minute resolution. Images are centered at the *R/V Polarstern* and extend radially to a distance of 3 nautical miles (approximately 5.4 km).

2.5 Upper-ocean turbulence and current measurements

Ocean timeseries observations were made from Autonomous Ocean Flux Buoys (AOFBs; Stanton et al., 2012) adjacent to the CO Met Tower and from the three L-sites. Each of these buoys supported a 4 m deep eddy-correlation turbulence sensor package providing direct heat, salt and momentum fluxes every 2 hours from 35-minute ensemble co-spectra of the 2 Hz sampled 3-component velocity, temperature and conductivity timeseries. Ocean friction velocities $u_o^* = (\langle u'w' \rangle^2 + \langle v'w' \rangle^2)^{\frac{1}{2}}$ from these co-spectra are used to infer the upper ocean stress ($\rho_o {u_o^*}^2$) at 4 m. A co-located Acoustic Doppler Current Profiler (ADCP) measured current profiles from 6 m to 80 m depth sampling every 2.5 s and every 2 m in depth, and reporting 15-minute ensembles with <1 cm s^{-1} noise levels. Earth-referenced absolute current profiles were calculated from the instrument-coordinate ADCP measurements by first rotating the component profiles into true north coordinates using declination-corrected fluxgate compass measurements in the ADCP and flux package, and, where possible, comparison with shipboard and ASFS GPS-based heading observations. The AOFB / ice floe horizontal motion was then removed using the AOFB GPS timeseries to form absolute u/v vector current profiles.

In this study, we use ocean measurements from the CO site adjacent to the main Met City tower. Water density profiles were calculated from the intermittent ship CTD and microstructure profiling program at the CO. Difficult operating conditions during this period of very high winds limited CTD sampling at the CO to as little as once per day. Seasonal mixed layer depths are estimated from the depth in each profile where there is a 0.2 kg m^{-3} potential density increase from the 8 m near-surface values. These sparse-in-time mixed layer depths are linearly interpolated in time and smoothed with a 12-hr period running average filter to estimate the depth of the top of the strong halocline observed across much of the Arctic. A much more sensitive density threshold of 0.01 kg m^{-3} is used as an indicator of the base of the active surface boundary layer in the analysis in section 5.

3 Atmospheric structure and evolution

3.1 Synoptic evolution

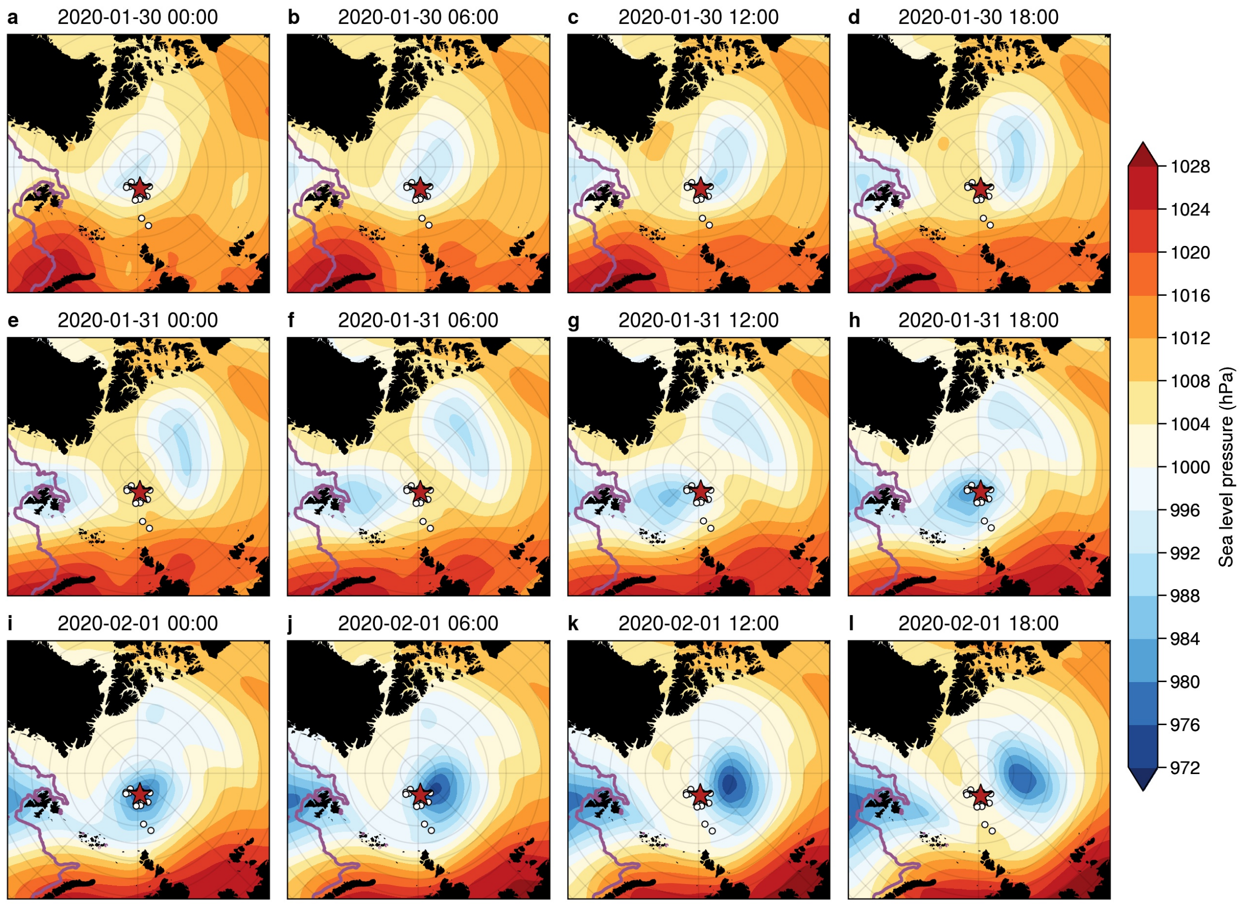

Figure 2. Sequence of ERA5 mean sea-level pressure (SLP) analyses at 6-hour intervals from 30 January 00:00 UTC to 1 February 18:00 UTC. The red star indicates the location of the CO, and the white circles show the buoys in the DN and ExDN. The position of the ice edge from the daily NSIDC 12.5 km AMSR2 sea ice concentration (SIC), defined as the 15% SIC isopleth, is indicated with a purple line.

Two cyclones crossed the MOSAiC domain in short succession between January 29th and February 1st, 2020 (Figure 2). The first cyclone (C_1) developed along the NE coast of Greenland on 29 January, strengthening slightly as it moved northward over the North Pole (Figure 2a-c). Soundings at the *R/V Polarstern* suggest that a warm front/cold front couplet developed with the system (discussed in Section 3.2) and that the warm sector passed over the MOSAiC domain. As this first cyclone was passing the MOSAiC domain, a second cyclone (C_2) developed along the west coast of Svalbard on 30 January and strengthened along Svalbard's north coastline as it moved northward (Figure 2c). While C_1 only deepened by about 7 hPa along its track, C_2 deepened by nearly 20 hPa, becoming one of the deepest cyclones to pass over the MOSAiC domain during the year (Figure 2i). The observed SLP minimum (974 hPa) in the MOSAiC domain during C_2 was 4 hPa lower than the minimum central pressure in the ERA5 fields, indicating that the observed cyclone was slightly stronger than in ERA5. A warm front/cold front couplet also developed with this system, both of which passed over the MOSAiC observatory.

3.2 Key mesoscale structures

Figure 3 shows an atmospheric frontal analysis of C_2 based on the 6-hourly ERA5 mean sea-level pressure, 10 m wind vectors, 925 hPa equivalent potential temperature (θ_e), and 950 hPa wind speed. In this and following figures, references to cardinal directions are relative to the CO. The polar stereographic maps are oriented so that north from the CO is in the positive *y* direction and east is in the positive *x* direction; note that the North Pole is 267 km north of the CO, so the direction of true north will vary substantially throughout the figure. The storm deepened by 8 hPa during the 18 hours shown and has clear spatial structure, with northward warm-air advection in the warm sector primarily to the right of the storm track ahead of the low center and southward cold-air advection in the cold sector primarily to the left of the storm track and behind the low center. The surface warm front passes over the CO (red star) on 31 January between 14 UTC and 16 UTC (Figure 3a), while a cold front aloft passes over the CO on 31 January near 23 UTC and a surface cold front passes over the CO near 02 UTC. The surface low passes very close to the CO but just to its west and north, such that the CO is initially in the warm sector air before being affected by the trailing surface cold front. Strong low-level wind speeds indicating a low-level jet (LLJ) initially occur in the warm sector between the warm front and the cold front aloft. By 1 February 00 UTC (Figure 3b), a LLJ (indicated here by the 16 m s^{-1} isotach at 950 hPa) encircles the surface low and remains as a nearly axisymmetric annulus through the rest of the time period as the system occludes with bands of warm and cold air wrapping around the low center (Figure 3c,d). Figure 2 suggests that C_2 was more axisymmetric (circular) than C_1. While C_2 is quasi-axisymmetric initially and becomes even more axisymmetric as it strengthens, C_1 starts out more elongated and becomes even more so with time. C_1 appears eventually to be absorbed into C_2. We hypothesize that the symmetry of the storm is an important factor in the development of the axisymmetric mesoscale LLJ annulus.

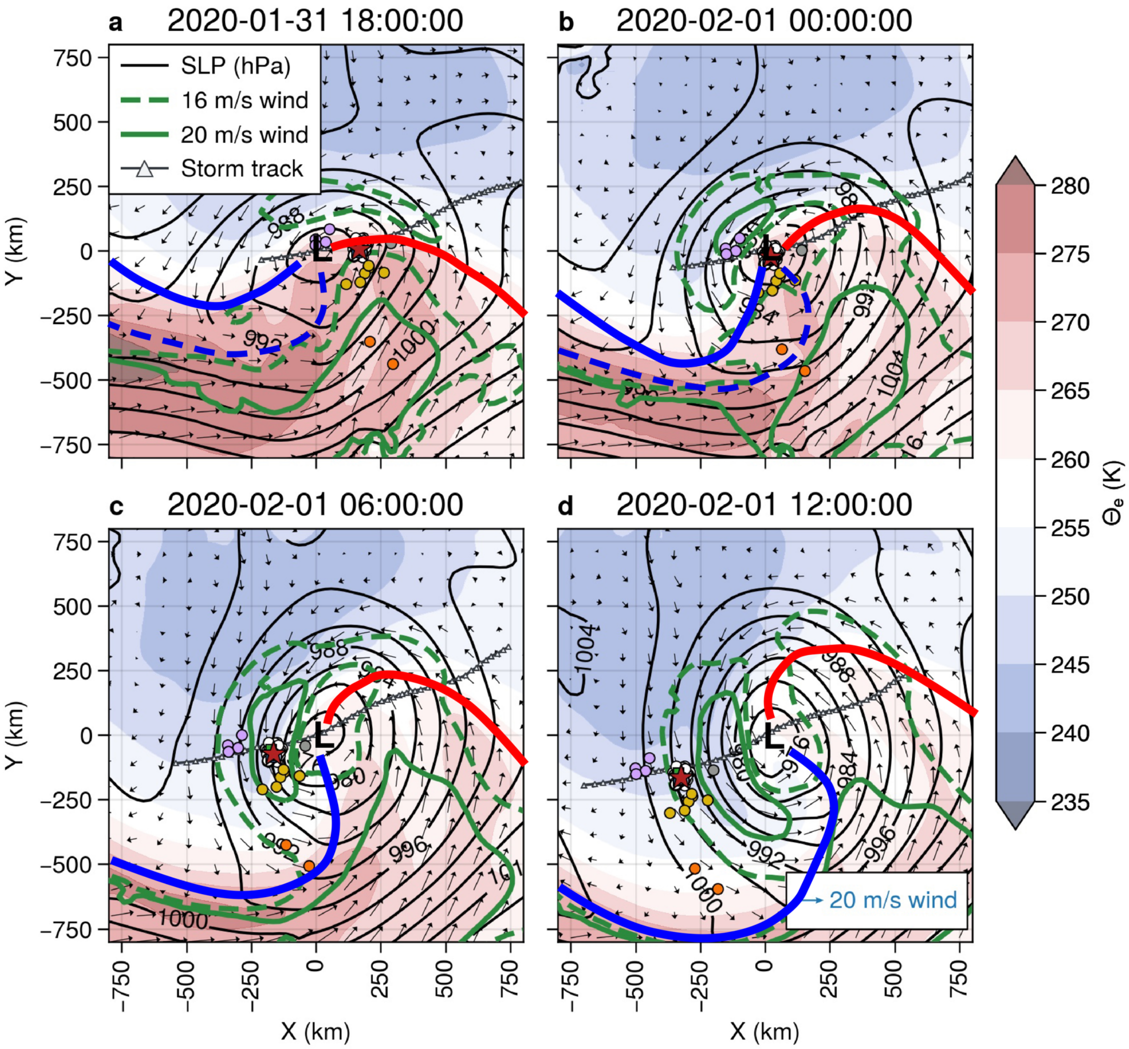

Figure 3. ERA5 reanalyses centered on the SLP minimum for cyclone C_2. Shown are SLP (hPa; black isopleths), 925 hPa equivalent potential temperature θ_e (K; colors), 10 m wind vectors, and select 950 hPa isotachs (16 and 20 m s^{-1}; green). Every fourth wind vector is plotted for clarity; vector length is proportional to wind magnitude. The heavy red and blue lines show the positions of the warm and cold fronts, respectively. Dashed front lines indicate thermal features aloft, while the solid lines depict fronts at the surface. The light gray line shows the track of the low

center within the domain, while the colored circles show buoy positions. Colors for DN and Ex DN sites are as in Figure 1.

Utilizing the near-surface observations at the three ASFS sites and at the CO, rough observational surface analyses are possible on the ~50 km scale of the DN. Figure 4 shows isotherm analyses centered on the CO between 31 January 14:05 UTC, just prior to the passage of the surface warm front, and 1 February 06:41 UTC, nearly 5 hours after the passage of the surface cold front. These are overlaid on low-elevation radar-reflectivity PPI scans to provide an indication of the spatial distribution and structure of the clouds (< ~0 dBZ) and precipitation (> ~0 dBZ).

Moderate (5-10 m s^{-1}) southeasterly surface winds were present throughout the domain as the air temperatures warmed with the approaching surface warm front (Figure 4b). Within the warm sector, temperatures gradually warmed to -11 °C. Winds were initially moderate from the SSW but decreased in magnitude as the low-pressure center neared the CO, particularly after the cold-front aloft passed overhead. The more cellular nature of the clouds and precipitation after the cold front aloft passed can be seen in comparing Figure 4c and 4d. The trailing surface cold front entered the DN from the NW, marked by a sudden wind shift to the N and a trailing, very strong temperature gradient (Figure 4e-g). Air temperatures dropped to between -27 °C and -30 °C. The cold front took about 1.5 h to traverse the L-site triangle. The northerly winds increased throughout this frontal zone, reaching near-surface speeds of 12-15 m s^{-1} as the LLJ behind the front passed overhead (Figure 4h-i). High wind speeds combined with strong cold-air advection leads to strong mixing near the surface, producing what appears to be horizontal roll vortices in the atmospheric boundary layer (suggested by the linear, along-wind, cloud and precipitation features). Horizontal roll vortices are an effective mechanism for vertical mixing in the atmospheric boundary layer (Etling & Brown, 1993; LeMone, 1973).

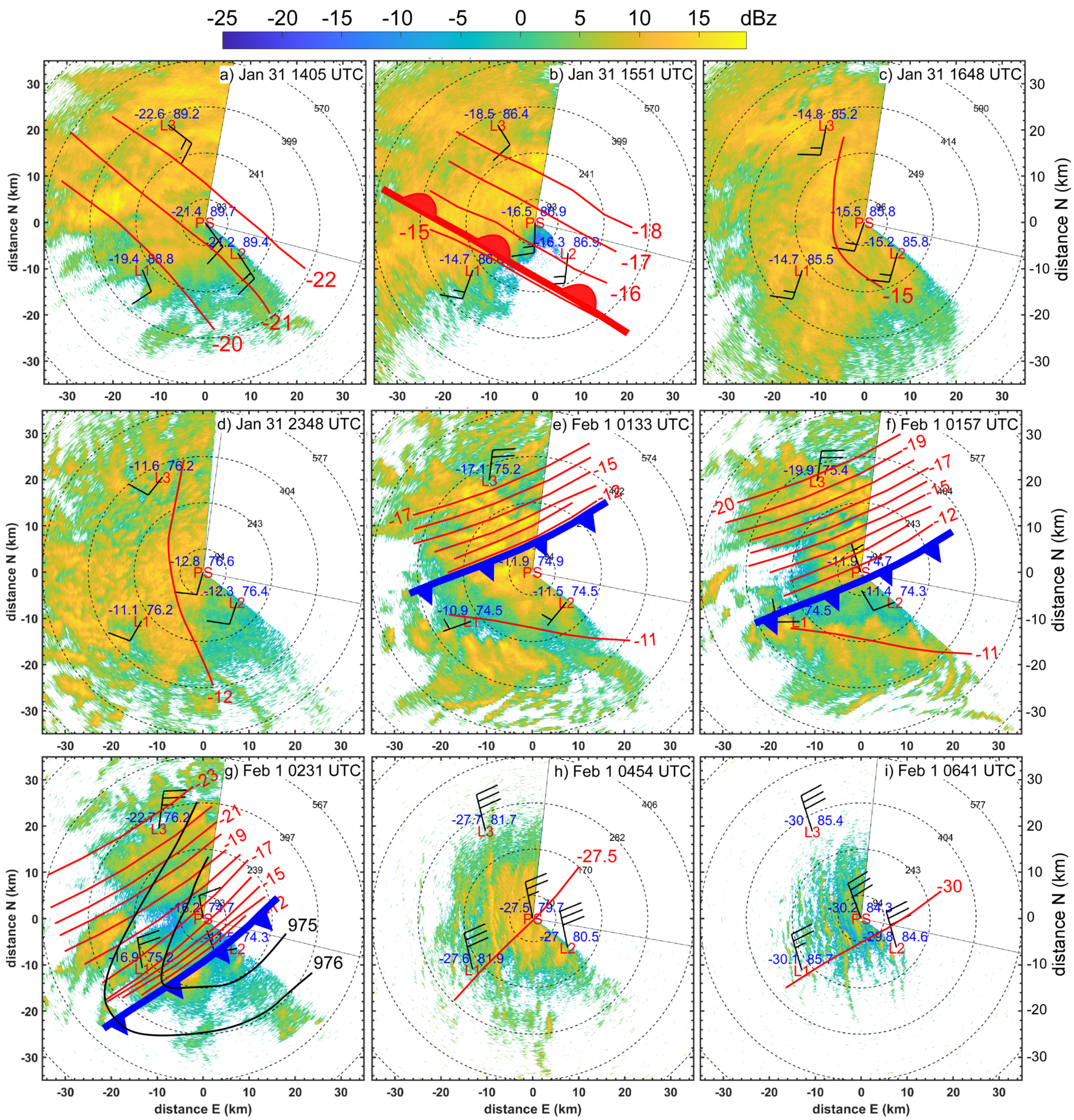

Figure 4. Near-surface meteorological observations of air temperature (°C), SLP (hPa), downwelling longwave radiation (W/m2) and wind barbs from the three L-site ASFSs (3.8 m) and at Met City (6 m)) during the warm-frontal (heavy red, lobed line) passage on 31 January (a-b), cold frontal (heavy blue toothed line) passage on 1 February (e-g), and in the post-cold-frontal sector (h-i). Manual analysis of air temperature is shown in red lines with 1°C isotherm interval. Panels with only one isotherm represent times when the spatial temperature difference between sites is less than 1°C. Isobar analysis is depicted with black lines in panel g. The

background shows PPIs of the low-elevation scanning Ka-band radar reflectivity (color, dBZ). Range rings (black dashed lines) are shown at 5, 15, 25, 35, and 45 km distances, and are labeled with the radar-beam height (m) above the local surface. The thin black radii bracket the region not scanned by the radar. North is upwards for each panel.

A time-height section of serial rawinsonde data and near-surface time series of various parameters (Figure 5) confirm the features passing over the MOSAiC domain discussed above. The passage of the first cyclone (C_1) and its associated narrow warm-sector are clearly seen, with the brief but distinct warm air peak in the warm sector, and the cooling and veering of the surface wind with the passage of the cold front. A LLJ is present at approximately 250 m above the surface near the time of the warm-frontal passage. The second cyclone (C_2) is deeper with a broader warm sector over the CO. The air warms only slightly in the warm sector between the warm front and the cold front, but the thermal wind effect from this thermal gradient, with the warmest air closest to the cold front, is a likely cause for the observed LLJ within the warm sector at 250-300 m height. The rawinsondes show the warm-sector LLJ wind speed maximum near 15 m s^{-1} just above the surface mixed layer (SML), with associated near-surface wind speeds of 7-8 m s^{-1} (Figure 5a, d; Figure 4c).

The passage of the cold front with C_2 near 02 UTC on 1 February marks the time of the lowest observed central pressure (974 hPa), a very sharp drop in surface temperature (-11°C to -38°C in only 12 h), a minimum in surface winds, and a rapid change in surface wind direction (Figure 5b-e; Figure 4e-g). A second LLJ is observed at ~350-400 m height just behind the cold front with a core speed of 21-22 m s^{-1} and with temporarily deeper SML as indicated by the constant θ_v with height. Just after the cold-frontal passage, the near-surface wind speed increases with the arrival of the LLJ above, reaching speeds of 14-16 m s^{-1} across the four observational sites between 04 and 06 UTC on 1 February (see also Figure 4h-i). The timing differences in the wind direction shifts, wind speed increases, and temperature decreases between sites (Figure 5d-e) represent the progression of the cold front across the DN from the northwest. Stability differences in the sub-jet layers may cause the higher surface wind speed relative to its core strength for this second post-cold-frontal LLJ when compared to the warm-sector LLJ. A peak in the observed covariance surface stress (τ_a) at Met City (Figure 5f) occurs just after the cold frontal passage, and is coincident with the deepening of the SML just below the LLJ (Figure 5a) and the appearance of the likely horizontal roll vortices (Figure 4h-i). It is unclear whether enhanced turbulence caused by the LLJ or the roll vortices have deepened the SML, or if the deeper SML has weakened the near-surface winds thereby producing a LLJ just above the SML. All of these features indicate significant, efficient, vertical momentum transport at this time.

The presence of the LLJ behind the cold front is likely due to the LLJ being quasi-axisymmetric around C_2. This "wrap-around" LLJ is likely an extension of the LLJ observed in the warm sector as this warm air wraps around the strong but compact cyclone center, as seen in Figure 3a-d. Note that the cold sector LLJ is at a slightly higher altitude than the LLJ in the warm sector, consistent with some lifting as the LLJ has wrapped itself around the cyclone center. There is likely a thermal wind contribution over a ~100 m deep layer at the core of this second LLJ. We infer that the presence of two LLJs in fairly rapid succession, possibly parts of a wrap-around LLJ within a rapidly moving cyclone, produces strong, rapid surface wind speed and wind direction changes as it translates across the MOSAiC domain. This is the key forcing for the significant ice motion, ice deformation and upper-ocean current changes observed during the passage of C_2. Such a double LLJ (wrap-around LLJ) was also observed in other MOSAiC cyclones with significant ice deformation (e.g., Persson et al., 2023).

Low-level atmospheric divergence is one way to quantify these wind transitions. Indeed, we observe significant atmospheric convergence with the passage of the warm and cold fronts of cyclone C_2, with the strongest convergence (~30 x 10^{-5} s^{-1}) occurring with the cold-frontal passage (Figure 5g). Ice convergence and shearing also show peaks. There is no appreciable ice divergence/ convergence within the L-site triangle associated with the warm frontal passage, though there is significant shearing of the ice (Figure 5g). Note that other substantial wind transition events also show some atmospheric divergence/convergence and some ice deformation (e.g., near 08 UTC on 3 February, also associated with a LLJ). Nevertheless, ice deformation events can have multiple local and nonlocal causes, and therefore are only sometimes associated with local atmospheric divergence.

445

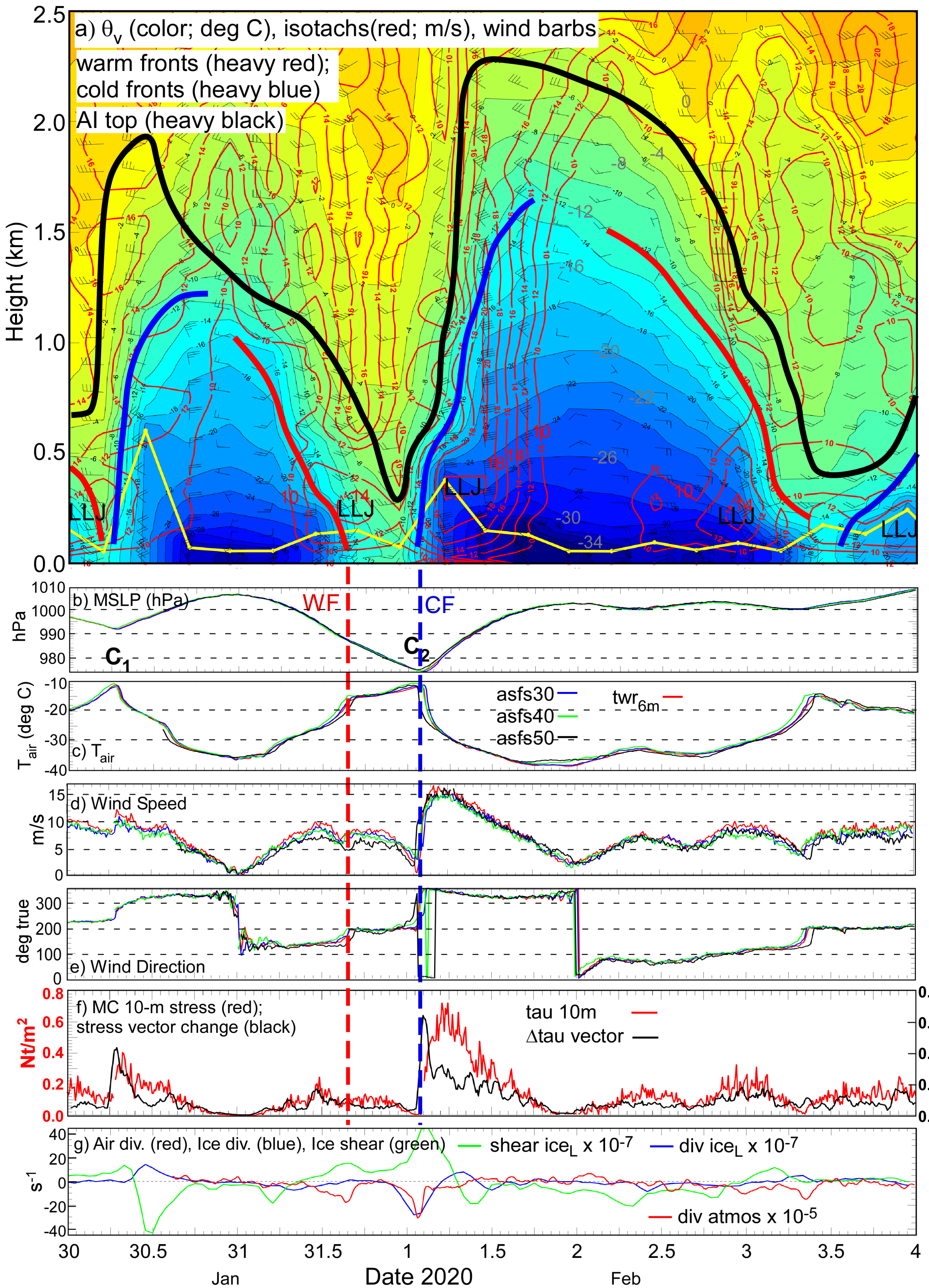
a) θv (color; deg C), isotachs(red; m/s), wind barbs
warm fronts (heavy red);
cold fronts (heavy blue)
AI top (heavy black)
Height (km)
LLJ
WF
CF
b) MSLP (hPa)
hPa
C1
C2
c) Tair
Tair (deg C)
asfs30
asfs40
asfs50
twr6m
d) Wind Speed
m/s
e) Wind Direction
deg true
f) MC 10-m stress (red);
stress vector change (black)
tau 10m
Δtau vector
Nt/m2
Nt/m2/h
g) Air div. (red), Ice div. (blue), Ice shear (green)
shear iceL x 10-7
div iceL x 10-7
div atmos x 10-5
s-1
Jan
Date 2020
Feb

Figure 5. a) Time-height section of virtual potential temperature (θ_v colors; °C, gray labels), isotachs (red), and select wind barbs from serial rawinsondes at the *R/V Polarstern*. Heavy (red, blue, black) lines mark warm and cold fronts and the top of the Arctic inversion (base of the free troposphere), respectively. The thin yellow line marks the top of the surface mixed-layer. Low-level jets (LLJ) are also marked. Rawinsondes were launched every 6 hours, launch times indicated by the origin of the wind barbs. Lower 6 panels: Time-series from the Met City tower and the ASFSs of b) MSLP; c) T_a; d) 10 m (Met City) and 3.8 m wind speed; e) 10 m and 3.8 m wind direction; f) 10-m atmospheric stress (red), stress vector change (black) at MC; and g) 3.8 m atmospheric divergence (red), ice divergence (blue), and ice shear (green). The vertical dashed lines show the times when the warm (red) and cold (blue) fronts with the second cyclone pass over. C_1 and C_2 mark the minima in MSLP with first and second cyclone, respectively.

4 Sea ice dynamics

4.1 Atmosphere-ice interaction

Sea ice motion during the passage of the cyclones is broadly coherent with the time-varying wind forcing. The drift speed ratio (α, the ratio between the local drift and wind speeds) and net turning angle (θ, the difference between the local wind and drift directions) vary significantly over time (Figure 6e, f). Note that the wind velocity in ERA5 is in good agreement with the observed winds (dark and light blue arrows in Figure 6a-d). The drift speed ratio and turning angle are empirical measures of the relationship between the ice drift and the wind speed. In steady state free drift, θ is a function of the boundary layer structure and the ice surface roughness, and α is a function of the air-ice and ice-ocean drag coefficients and the densities of each medium. For the period shown in Figure 6e-f, average values of α and θ are 0.021 and 35, respectively, consistent with previous studies (Leppäranta, 2007; Schweiger & Zhang, 2015; Womack et al., 2022). Drift speed ratios are low in the warm sectors of both cyclones, while they increase after the arrival of the cold fronts. The turning angle in the warm sector is slightly larger than the mean for C_1, but below the mean for C_2. Drift speed ratio remains high after the cold front on 1 February, which suggests that a larger fraction of atmospheric momentum is being converted into ice motion rather than adding to the internal ice stresses. Increases in α following cyclone passage has been observed previously (e.g., Itkin et al., 2017). The drift speed ratio following the second cyclone passage oscillates near the inertial frequency (~12 hours), suggesting the possibility of inertial oscillations following the storm.

Drift trajectories of the three L-sites and the CO (Figure 6a-d) generally illustrate the expected right hand turning rule ($\theta > 0$) first noted by Nansen (1902). At all four sites, the ice drift arcs to the right and slows as the cyclone C_1 moves away from the MOSAiC site. During the passage of the pressure ridge between cyclones C_1 and C_2, the wind direction abruptly reverses (Figure 5e; Figure 6a-d). This reversal occurs at 23 UTC on 30 January at all sites, marked by the red letter A. As SLP decreases and C_2 approaches the CO, the ice drifts northward due to southerly winds until slowing to a halt and again reversing direction. The cusp in the trajectory marking the reversal is indicated by the letter B. Notably, this reversal precedes a rapid acceleration, and occurs at different times at each site: first at 22:30 UTC on 31 January at L3, next at 0 UTC on 1 February at sites L1 and at the CO (Met City), and last at 0:30 UTC on 1 February at L2. These times are all about 2 h prior to the passage of the cold front and the large change in wind direction at each site. Cusps in DN buoy trajectories are identified by local minima in drift speed. Cusp timestamps display a west-east gradient spanning a 3-hour period consistent with ~25 km/h (~7 m s^{-1}) cyclone propagation speed (Figure 7b), with some deviations likely due to propagating internal ice stresses from nonlocal forcing. That is, it appears as if the 2 h difference in wind and ice drift direction changes and the deviations in the propagation of the ice drift reversals may be due to internal ice stresses caused by non-local wind forcing behind the cold front. Further from the storm center, 48-hour drift trajectories show clockwise motion to the right of the storm (Figure 7c, d) and counter-clockwise motion to the left (Figure 7a), with the sharpness of the turn increasing nearer the storm center due to the smaller radii of the quasi-annular wind around the low center.

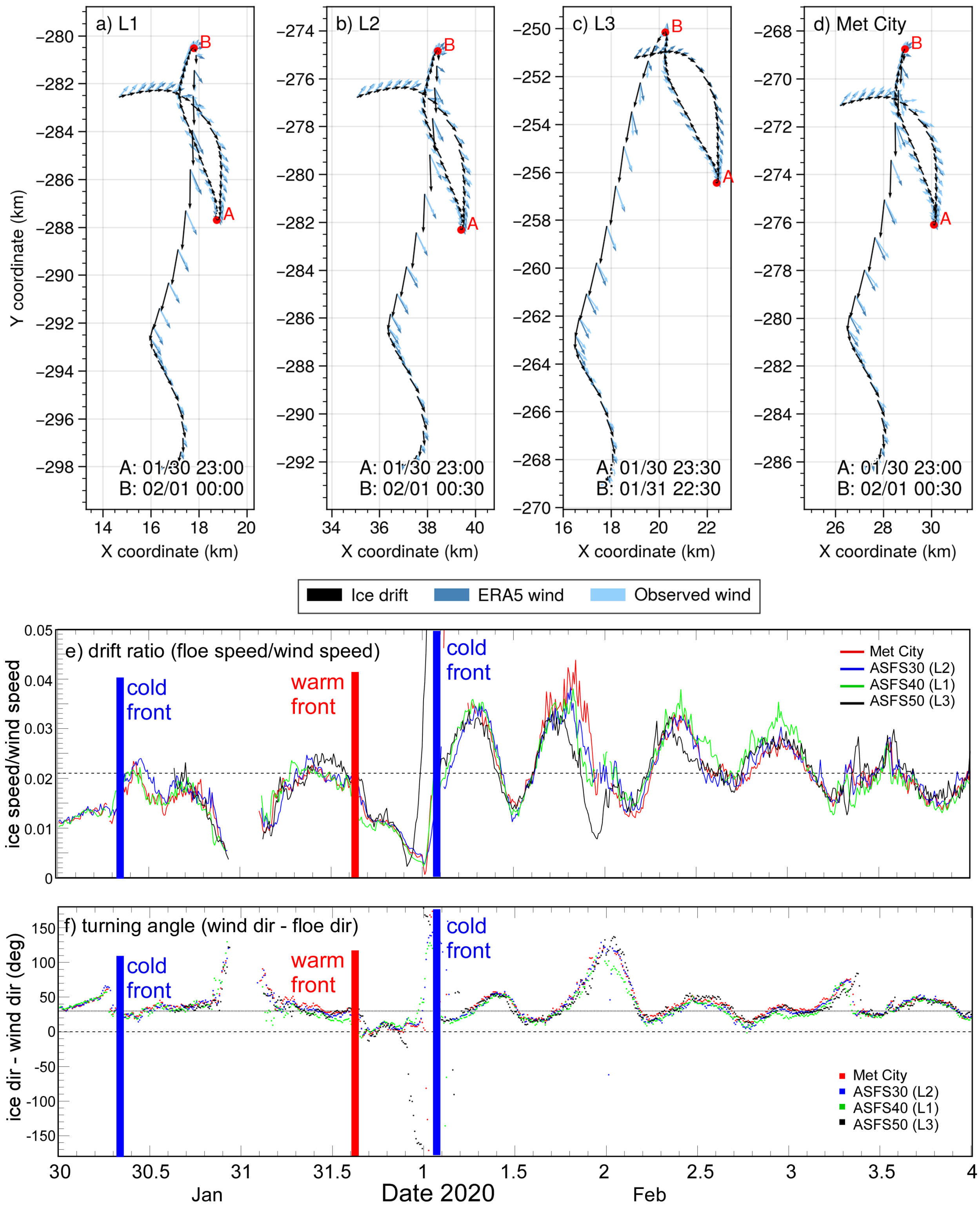

Figure 6. Top a-d: Trajectories of sites L1, L2, L3, and Met City at hourly resolution from 30 January 00:00 UTC on 02 February 00:00 UTC. Black arrows indicate the ice drift direction,

light blue the observed wind direction, and dark blue the estimated wind from the ERA5 reanalysis. Arrow length is proportional to speed; wind speeds are scaled to 2% for comparison with the drift speed. Bottom: (e) Drift speed ratio (ice speed divided by wind speed) and (f) empirical turning angle (difference between wind direction and ice drift direction) derived from 10-min wind and ice drift observations at sites L1, L2, L3, and Met City.

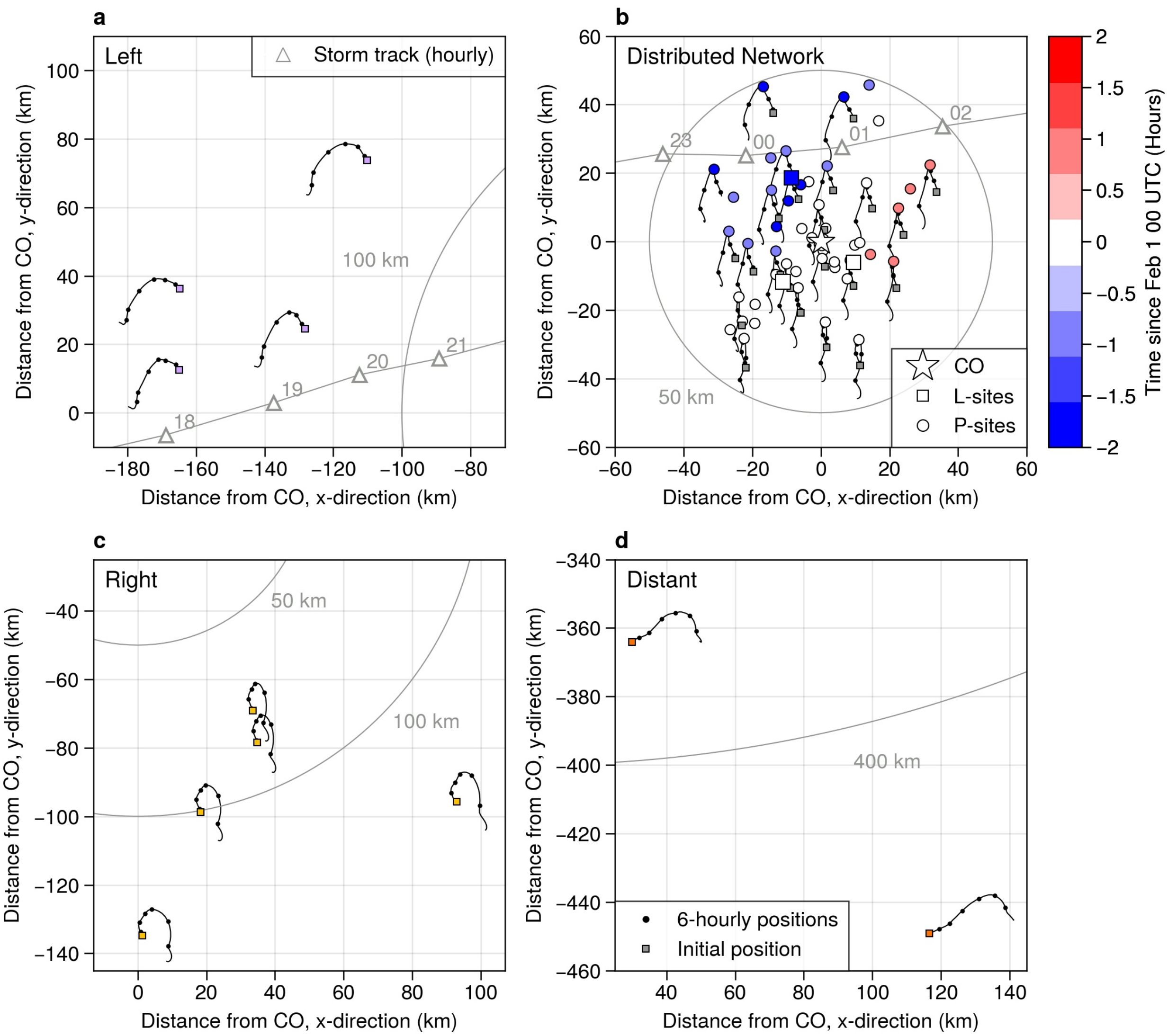

Figure 7. Buoy trajectories from 31 January 00:00 UTC to 2 February 00:00 UTC. Small squares indicate the beginning of the time series. Black lines show the 30-min resolution drift tracks, and black circles show the position every 6 hours. Distance from the CO is indicated with the axis units and radii at 50 km, 100 km, and 350 km. In panel b, the time of the drift speed

minimum relative to 1 February 00:00 UTC is indicated with color. Trajectories of a subset of DN buoys are shown for clarity. L-sites are marked with large squares, while the CO is marked by a star. In panels a and b, the position of the sea level pressure low from the ERA5 reanalysis is marked at hourly intervals with triangles and labeled with the corresponding hour of day.

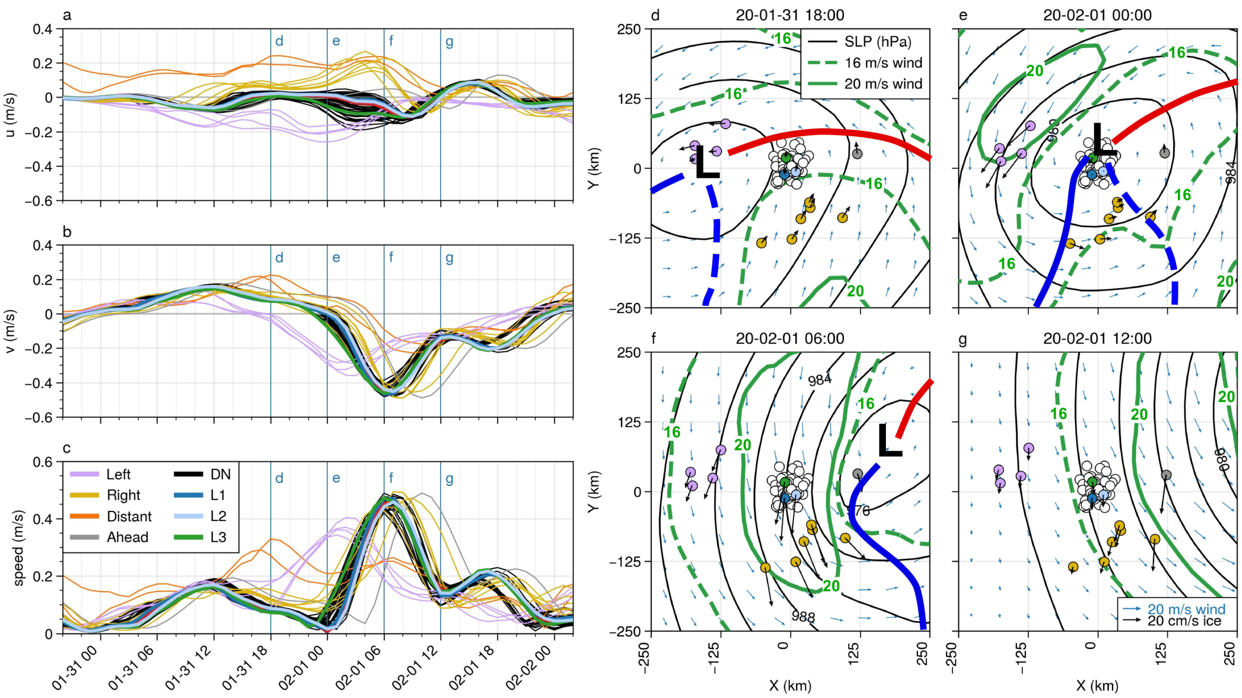

Figure 8. Left: Buoy velocity components (a, b) and magnitude (c) for the period from 30 January 20:00 UTC to 2 February 02:00 UTC. The top and middle panels show the u and v velocity components relative to the north polar stereographic projection, thus corresponding to the x and y axis, respectively, in the panels on the right. For the period shown here, the positive y direction is approximately northward. Right: Snapshots of buoy motion (thick black arrows) superimposed on the ERA5 sea level pressure isobars (black contours, 4 hPa spacing), near-surface (10 m) wind fields (blue arrows), and 16 and 20 m s^{-1} isotachs of the 950 hPa winds (green contours) at times corresponding to vertical lines in the velocity time series to the left.

The position of the SLP minimum is marked with "L". The cold front is marked in blue and the warm front is marked in red. Solid fronts are surface level and dashed are elevated.

The clearest sign of the storm's impact on the ice velocity is through the effect of the LLJ as it develops and moves across the MOSAiC array. High ice drift speeds indicate efficient downward mixing of momentum through the atmospheric boundary layer. Since buoy velocities were not assimilated in ERA5, coincident ice velocity and 950 hPa wind speed maxima (Figure 8d-g) serve as an independent confirmation that the location of the LLJ in ERA5 is approximately correct. During the second cyclone, the cold sector LLJ core first passes over the left buoy group (Figure 8e), where drift speeds reach an average speed of 37 cm s^{-1} between 01:00 and 02:00 UTC on 1 February (Figure 8c) under the LLJ core of >20 m s^{-1}. The DN buoys come nearly to a full stop before reversing direction and being accelerated by the cold sector LLJ (Figure 8c). Maximum speeds of 42-49 cm s^{-1} occur between 05:00 and 08:00 UTC on 1 February (Figure 8c) as the LLJ core passes overhead (Figure 8f). There is a larger spread in velocity between the DN buoys during this time, implying deformation. The DN buoys and the right group reach their maximum speeds at approximately the same time (Figure 8c, f) yet due to the wind curvature within the LLJ core, the direction of ice motion is different.

4.2 Sea ice deformation

Differential motion across the buoy array implies deformation. We measure this deformation by monitoring the changes in polygons formed by subsets of the buoy array (Figures 9, 10) and through examination of ice radar imagery (Figure 11). At moderate-to-large scales (purple, yellow, and black lines and polygons in Figure 9), the largest signals in strain rates can be understood as responses to the cyclone-scale wind gradients and the positions of the LLJ cores. As a band of high wind speeds is advected over the ice, the ice experiences changes in vorticity, divergence, and shear strain rate (Haller et al., 2014; Lindsay, 2002). For the LLJ behind the storm, the vorticity pattern is first cyclonic, accompanied by gradually increasing divergence (opening), then as the wind speed slows, the sense of rotation reverses, and the ice closes. This is seen on 1 February both for the purple (00 to 08 UTC) and black (04-11 UTC) polygons, but at slightly different times. Significant variability exists in the strain rates, particularly maximum shear strain rate, likely due to the complex interaction of the geometry of ice fractures and the varying wind forcing. The vorticity signal is broadly coherent (Figures 9c, 10c), with a clear peak in positive vorticity at 2-3 UTC on 1 February and a trough of strongly negative vorticity between 9-11 UTC on 1 February in all except the purple buoy group, which has the same positive/negative vorticity couplet except 6-8 h earlier. The cold-sector trajectory and different timing of the position of this buoy group relative to the LLJ core seen in Figure 9d-g likely explain this time difference. This coherent positive ice-vorticity signal should be expected from the presence of the narrow axisymmetric atmospheric LLJ annulus surrounding the cyclone. The positive vorticity signal as the storm approaches is damped because the LLJs developing in the warm and cold sectors of the storm had not yet joined, and the winds ahead of the low center were weaker than the winds behind it (cf. Figure 3).

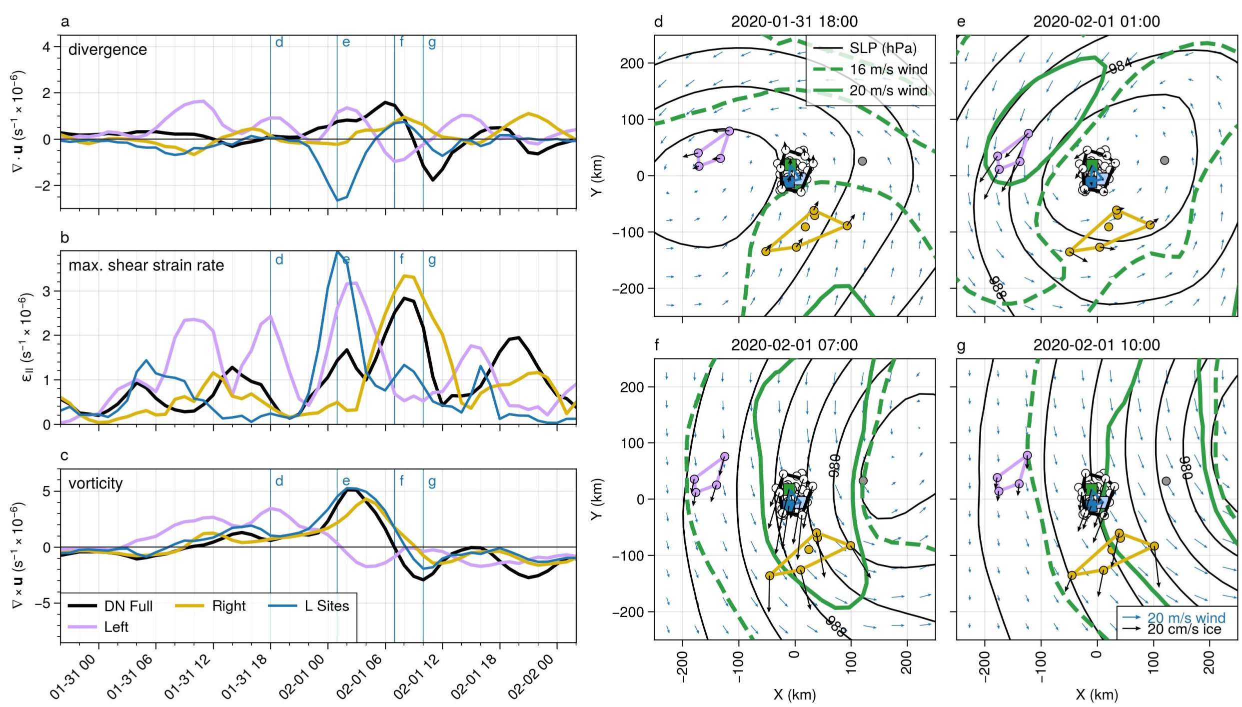

Figure 9. Time series of ice deformation components (a-c) and fields of 10-m winds, MSLP isobars, and 950 hPa isotachs (d-g) of the DN and Extended DN for the February 1 cyclone. Polygons used for the deformation calculations are shown in panels d-g. Polygons were selected

manually. Length scales are 57 km, 40 km, and 66 km for the DN Full, Left (purple), and Right (yellow) arrays, respectively, and 18 km for the L-site array (blue).

Within the DN, the small-scale polygons generally show ice deformation consistent with the DN Full polygon, with initial positive divergence as the LLJ core approaches the polygon. The importance of local fracture network structure in floe-floe interactions is demonstrated in the broad range of divergence values, and in the outlying behavior of the L-site triangle. Considering the wind field shown in Figure 9d-g and 10d-g, and the tendency of ice to move to the right of the wind, we expect opening (positive divergence) while the low is centered over the DN. In pack ice, individual floe motion is limited by interaction with neighboring floes, described as “multifloe” (~2-10 km) and “aggregate” (10-75 km) motions in the hierarchy proposed by McNutt and Overland (2003). The buoy velocity anomalies show that a region of at least 30 by 60 km is moving approximately coherently within the DN (Figure 10d-g). As the wind direction changes, the geometry of the interlocked floes results in different regions moving as aggregates. The passage of the cold sector LLJ, as indicated by the rise and fall of sea ice velocity, occurs within approximately 12 hours (00-12 UTC on 1 February). Differences in the ice motion due to the storm structure are visible at ~100 km (larger than “aggregate”) length scales, while significant deformation is occuring at ~10 km (“multifloe”) length scales. Remote sensing observations of ice drift are only rarely available at higher than 1 day resolution, and most products have spatial resolution between 25-75 km; typically, higher spatial resolution comes at a cost of smaller scenes and longer times between repeat observations (Sandven et al., 2023; Wang et al., 2022). Global-scale coupled model experiments have primarily been run on 0.25° or coarser grids (e.g., Long et al., 2021; Taylor et al., 2012). Thus, the strongest impact of the storm on the ice velocity and, especially, deformation is occurring at time and space scales shorter and smaller than many satellite ice motion observations and coupled model resolutions can resolve.

Within a consolidated ice cover, there is considerable resistance to ice opening, though some leads do open. As the winds recede, the newly opened leads offer little resistance to convergent motion. Thus, there is considerable spread in positive divergence across the DN polygons from 31 January 22 UTC to approximately 9 UTC on 1 February, while convergence after that time is faster and more cohesive across the set of polygons (Figure 10a). The position of shear zones can lead to ambiguity in area-average strain rates, as discussed in Lindsay (2002) (see also Bouillon & Rampal, 2015; Lindsay & Stern, 2003; Thorndike, 1986). The anomalous convergence shown in Figure 9a and 10a for the L-site triangle is an artifact of the triangle orientation relative to a shear zone that cuts through it. The shearing motion is a discontinuity in the ice velocity that leads to the triangle area to not be representative of the deformation, and compression is overestimated. The presence of this shear zone is clearly visible in the velocity anomaly map of Figure 10e. Higher confidence can be placed in the estimate of deformation from the DN Full array due to the larger number of buoys (vertices) used and larger area relative to shear zones. Over the 10-day period from 26 January 2020 to 5 February 2020, the area of the DN Full polygon changed from 3.17×10^3 km^2 to 3.21×10^3 km^2, a change of just over 1%. Rapid area increase (i.e., positive divergence) occurred on 1 February due to the passage of the cold sector LLJ from 00-09 UTC (Figure 10a), such that the area of the polygon increased by 3.5% in a 9-hour period, likely producing leads. Given that the surface air temperature was -10 °C or below during this period, any leads would have quickly begun freezing over. The resulting net increase of area over the 10-day period represents both thermodynamic ice growth in leads and mechanical redistribution of ice thickness in subsequent convergence.

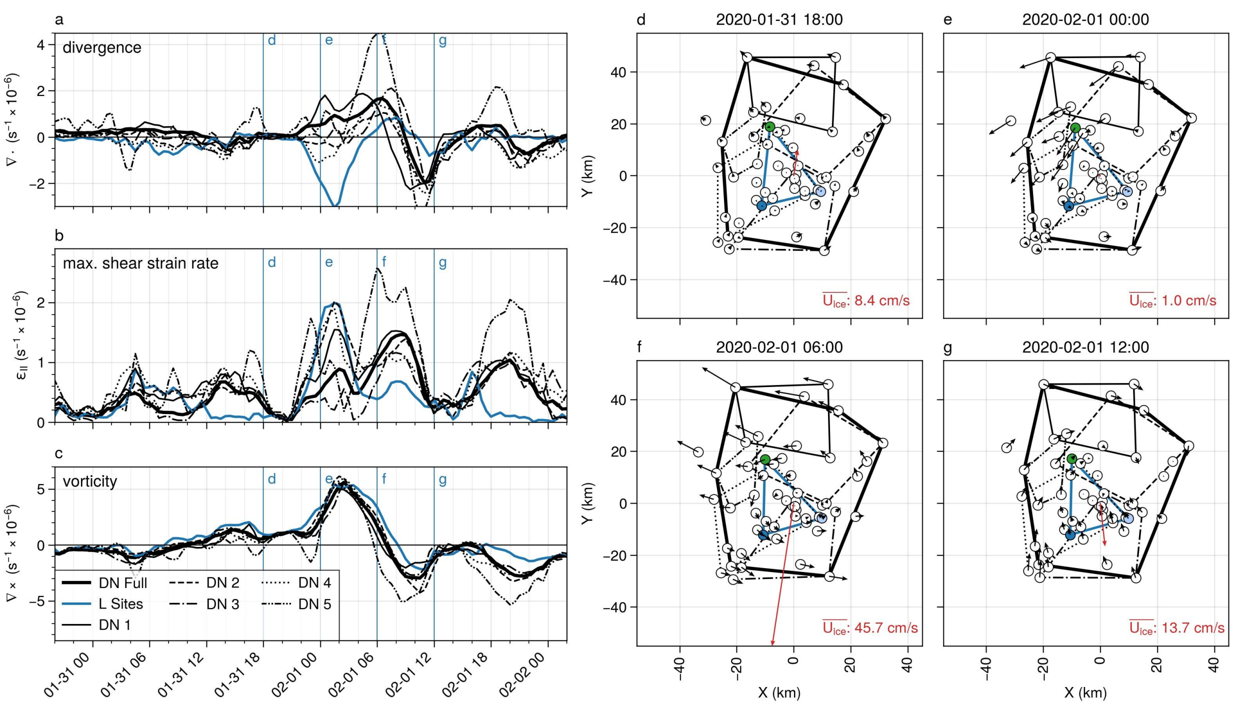

Figure 10. Time series of ice deformation components (a-c) and fields of buoy velocity anomalies (d-g) in the DN for the February 1 cyclone. Polygons used for the deformation calculations are shown in panels d-g; the polygons were selected manually. Note that the buoy in

the upper left was not included in the DN Full array due to periods of missing data. Velocity anomalies in panels d-g were computed relative to the ensemble average velocity, which is shown as the red arrow at the center of each panel with magnitude shown in the lower right. The length scales of the polygons (square root of the average polygon area) are 28, 33, 28, 30, and 15 km for DN sub-arrays 1-5 respectively, 18 km for the L-site triangle, and 57 km for the DN Full array.

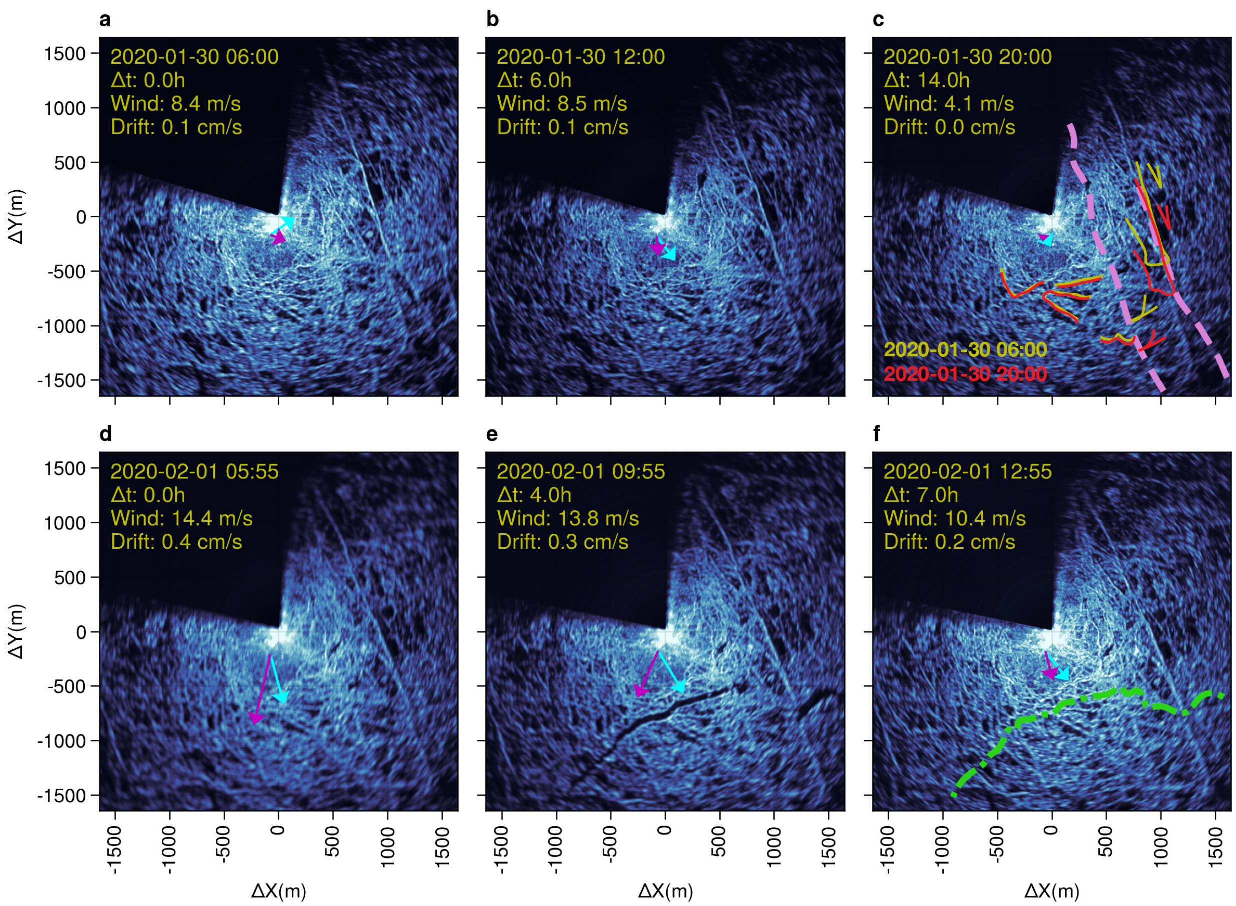

Figure 11. Backscatter from the ice radar on board the R/V Polarstern show small-scale deformation near the CO. The dark sector is blocked from the radar by the ship superstructure. Image date and time, wind speed, and drift speed are indicated in the upper left of each panel. Elapsed time (Δt) since the first image in each row is also indicated. Magenta and cyan arrows show the ice drift and wind directions at the Met City tower, respectively. Arrow length is

proportional to speed; wind speed has been scaled by 2% for comparison with drift speed. Annotations in panel c show the relative movement of manually identified ice features at 30 January 06 UTC (yellow) and at 20 UTC (red), revealing two prominent shear zones marked with the dashed pink lines. The green dashed line in panel f shows the location of a fracture that began opening at 1 February 07 UTC and closed by 13 UTC.

Ice radar images provide details of the ice deformation near the MOSAiC CO. Figure 11 depicts radar backscatter intensity which is related to sea ice roughness features. Dark areas in radar images are interpreted as undeformed level ice or leads. High backscatter (bright areas) arises from ridges and edges of leads. Relative motion of these features or their appearance/disappearance between images indicate ice shearing, the formation of leads or ridges, or the closing of leads. Motion is readily apparent in the 15-minute resolution animations of the radar images from 25 January at 00:00 UTC and 5 February 0:00 UTC provided in the Supplement, but in some cases can be discerned in side-by-side comparisons as in Figure 11. Note that the radar is located on the roof of the bridge of the *R/V Polarstern*, located at the apex of the unsampled dark area towards the stern of the ship at the center of each image. All depicted ice motion is relative to the radar.

The first row of images illustrates the shearing that occurred between 06:00 and 20:00 UTC on 30 January, as cyclone C_1 passed north of the DN. During this time, the group of highlighted bright features to the right of the dashed line moved southward relative to the *R/V Polarstern* (Figure 11c). Most of the shear was concentrated in two regions indicated with pink dashed lines. Both shear zones had been activated at least once in the week prior. During this event, shearing began at the right-most shear zone at 06:00 UTC, then along the left shear zone at 09:50 UTC. This shear zone activated again between 22:00 UTC on 31 January and 00:00 UTC on 1 February, corresponding to the peak in shear near 23:00 UTC on 31 January in Figure 10b, and corresponding to the approximate time that the ice motion at the CO and L-sites reversed (Figures 6a-d). These local details corroborate the deformation measured with the DN buoys (Figure S1); the southward motion anomaly is coherent across a region of at least 30 by 30 km.

The ice divergence maximum occurring near 06:00 UTC on 1 February in Figure 10a is also apparent in the ice radar data (Figure 11d-f). Starting at 07:00 UTC on 1 February, a fracture activates 1.5 km to the south of the *R/V Polarstern* (green dashed line in Figure 11f), reaching a maximum opening near 10 UTC. Two leads are formed with maximum width of 100-200 m, separated by a shear zone (black patches in Figure 11e). The leads are open only briefly, closing by 12:55 UTC. This time period corresponds to the period of large atmospheric stress (Figure 5f) and the atmospheric horizontal roll vortices (Figure 4h-i). Note that Figure 10a shows ice convergence occurring between 09:00 UTC and 13:00 UTC on 1 February, in excellent agreement with the ice radar observations. These abrupt ice motions are more easily seen in the animation of images at 15 minute resolution between 25 January at 00:00 UTC and 5 February 0:00 UTC presented in the Supplement.

Together, the drifting buoy data and ice radar data together show a consistent and complementary picture of sea ice response to synoptic and mesoscale features of the atmospheric wind structure. The passage of mesoscale features in the wind field (fronts and LLJs) exerts stress on the sea ice, resulting in deformation. The spatial coherence of the sea ice response is determined both by the scale of the wind forcing and by the geometry of local fracture networks. We therefore can expect that the significant transfer of momentum from the atmosphere into the sea ice results in a strong momentum flux into the upper ocean.

5 Upper ocean response to sea ice motion

Comparisons between the wind, ice and earth-reference current speeds at 8, 20 and 60 m depths (Figure 12a) summarize the transfer of momentum from the atmosphere, to the ice, and then to the ocean. This timeseries is dominated by distinct wind events on 30 and 31 January, and the strong transient event early on 1 February (Figure 12a; see also Figure 5). Each wind event accelerates the ice, which in turn accelerates the ocean layer below the ice as the turbulent ocean Ekman boundary layer forms. This can most clearly be seen in the 1 February event when wind magnitude dropping to near zero, within the annulus of the atmospheric LLJ, followed by an increase to 16 m s^{-1} in the following few hours. A local maximum ice velocity of 0.5 m s^{-1} lags the wind speed peak by 3 hours, while a 0.27 m s^{-1} current speed maximum at 8 m depth lags the ice speed maximum by ~1 hour compared to ~2 hours at 20m depth. These temporal lags are a result of the inertia of first the surface wind stress accelerating the ice, and then the depth-dependent acceleration of the upper ocean as the ice-ocean turbulent boundary layer deepens in response to changes in direction and magnitude of the ice motion.

Rapid changes in ice speed and direction during this event also force significant levels of circular inertial motion in the coupled ice-ocean system. This can be seen in the dampened oscillatory current components in the north-south and east-west velocity timeseries in Figures 12c-d, starting near 1 February at 06:00 UTC and continuing for over 2 days, with the inertial ringing decaying over time. The observed ocean currents represent a superposition of inertial ringing and the evolving boundary layer currents forced by the 1 February 02:00 UTC wind event and subsequent smaller wind maxima at 12:00 UTC on 2 February and 00:00 UTC on 3 February. The inertial ringing is a resonant response to the combination of sharp transient lateral accelerations of the ice/upper ocean coupled with the orthogonal Coriolis acceleration. They are widely observed in the Arctic, with higher magnitudes seen in high open water fraction conditions where ice mobility is enhanced (for example, Brenner et al., 2023). For this event, the 8 m depth east-west currents track the ice motion very closely (Figure 12a) with a small phase lag and reduced current component magnitude at 20 m, while the north-south component shows an inertial response from the ice down to at least 20 m but with a larger mean boundary layer current superimposed during 1 February. As expected, there is little direct coupling of this inertial motion at depths below the seasonal (~40 m deep) mixed layer as seen in the 60 m depth time series (Figure 12a); the strong density jump at the base of the seasonal mixed layer greatly reduces mixing and hence momentum transfer to greater depths.

Comparison between atmospheric surface stress and 4 m ocean stress during this period (Figure 12e) shows a deficit on the ocean side of the ice. There are two primary reasons for this difference. The first is the ability of the ice pack to remove surface-imposed momentum through a combination of internal ice stresses and ice deformation. The second is the important role of form drag from the MOSAiC ice pack. The momentum transferred by ice keels and floe edge features is not captured by the friction velocity u_o^* which arises from upstream, small scale roughness features across the ensemble of ice floes and generates the turbulent ocean boundary layer. Lags between the peaks of atmospheric stress and ocean stress, most clearly seen in the strong 1 February event, arises from the inertial lag of the ice pack to surface wind stress (Figure 12e).

The vertical structure of upper ocean currents in response to this wind event (Figure 13) illustrates the fairly complex interaction of the ice/ocean boundary layer with weakly stratified mesoscale ocean features within the seasonal mixed layer, which were seen during much of the

MOSAiC transpolar drift. High temporal resolution vertical shear of the N/S current component sampled every 15 minutes by the AOFB current profiler at the CO (Figure 13c) provides some insight into the complex structure of the active mixing layer. CTD profiles were limited by wind conditions and as such are sometimes only available once per day. Ideally, CTD profiles at a comparable temporal resolution to the AOFB current profiler would show the evolution of stratification within the mixed layer, which frequently contained weak mesoscale density structures limiting the depth of mixing during wind events. However, the much higher resolution shear profile time series in Figure 13c reveal both the development of strong near-surface shear as the sub-ice Ekman layer forms, and the development of regions of higher shear within the ~40m deep seasonal mixed layer. These shear layers indicate the lower extent of the mixing layer where even weak density gradients inhibit turbulent mixing deeper within the seasonal mixed layer. Measurements of these weak stratification layers are estimated from the depths where there is a density increase of 0.01 kg m^{-3} from surface values for each CTD profile, and are plotted as filled red circles in Figure 13c. These sparse-in-time observations coincide with the layers of increased shear measured in the current profiles. The red mixed layer depth timeseries in the Figure 13 panels represent coarse interpolated estimates of the depth of the top of the halocline.

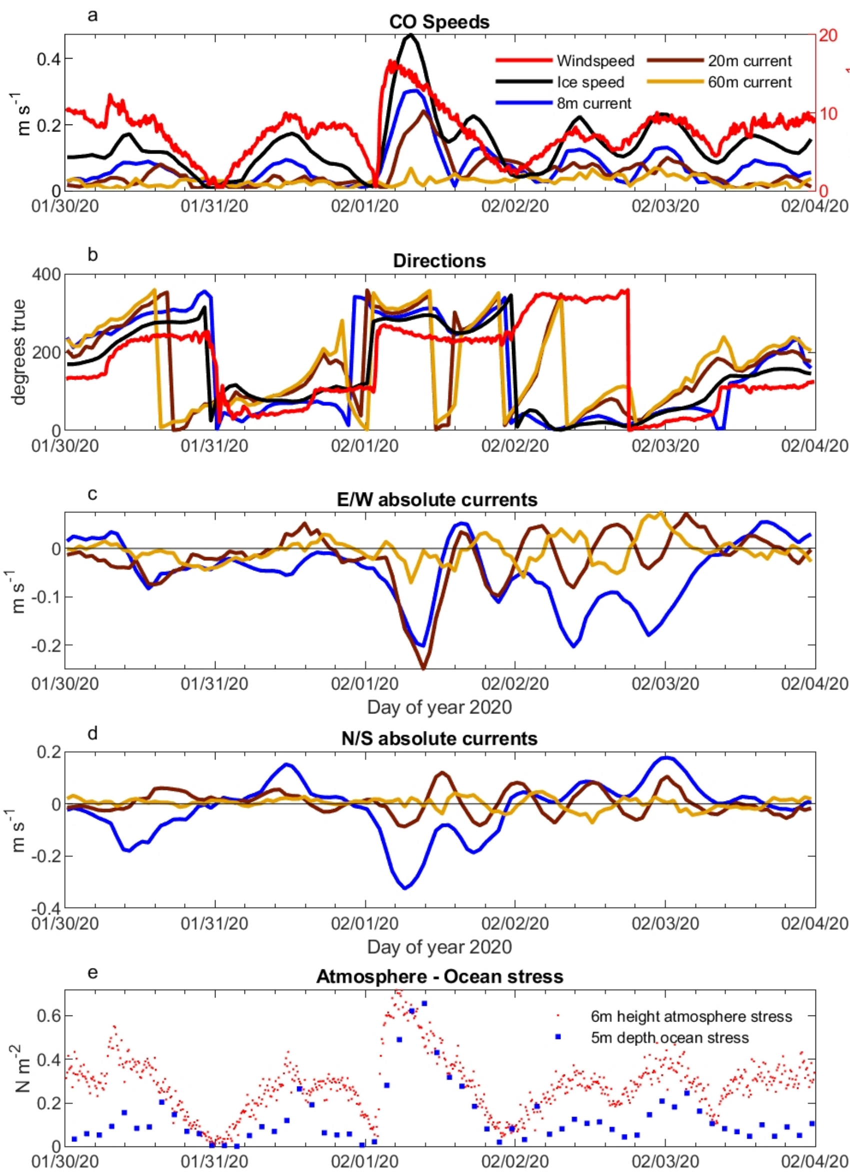

Figure 12. From top to bottom: (a) Timeseries of windspeed (red), ice speed (black), 5 m (blue) 20 m (green) and 60 m (orange) depth absolute current magnitude; (b) Corresponding current and wind directions in degrees true; (c) Timeseries of 5 m (blue), 20 m (brown) and 60 m (gold) north-south current components; d) east-west current components; e) 4 m depth ocean kinematic

stress from the CO site Autonomous Ocean Flux Buoy (blue dots) and atmospheric stress (red dots) for this study period.

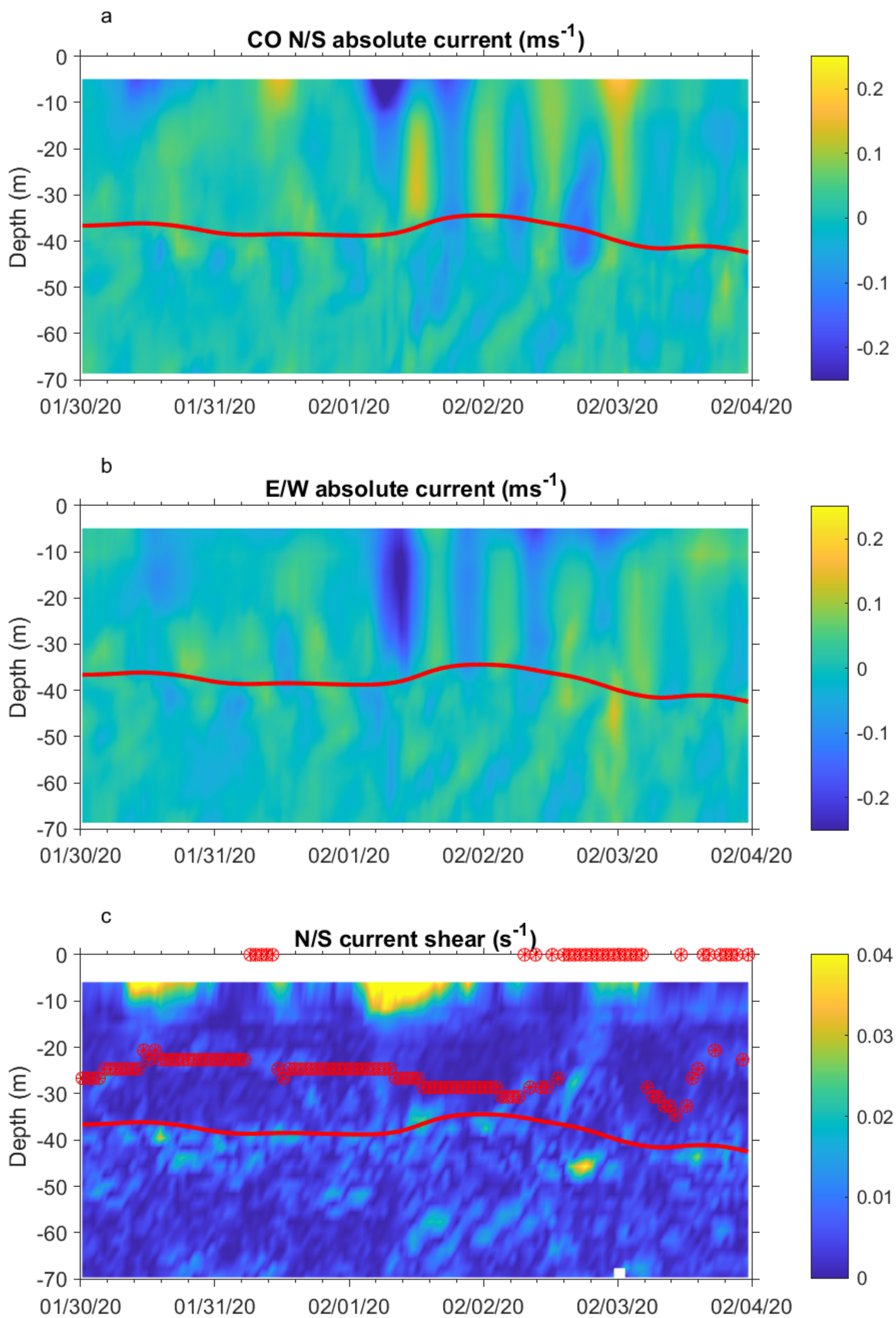
a
CO N/S absolute current (ms-1)
Depth (m)
0
-10
-20
-30
-40
-50
-60
-70
01/30/20
01/31/20
02/01/20
02/02/20
02/03/20
02/04/20
0.2
0.1
0
-0.1
-0.2
b
E/W absolute current (ms-1)
c
N/S current shear (s-1)
0.04
0.03
0.02
0.01
0

748

Figure 13. North-south current profile timeseries from the L1 site Autonomous Ocean Flux Buoy acoustic Doppler profiler. b) Corresponding East-West current component profiles. c) North/South current shear profiles with a clipped color scale to emphasize shear layers within the ocean mixed layer and upper part of the salinity-stratified pycnocline. Near surface shear reaches 0.07 s^{-1} during the 1 February wind event. The continuous red line represents an estimate of the depth of the top of the halocline. The sloping orange line highlights the rapid penetration of mixing in response to this wind event. The four black sloping lines identify shear associated with inertial internal waves within the strongly stratified pycnocline forced by the strong inertial motions within the ocean mixed layer.

The highest vertical shear levels of the north/south current component (Figure 13c) are seen in the upper 15 m during the strong 1 February wind event. However, active mixing extends down through the seasonal mixed layer to the halocline seen most clearly in the E/W current profile (Figure 13b) and the elimination of shear at the weak stratification interface between 20 m depth and the halocline (marked by the orange line in Figure 13c). An example of reduced mixing depth by a mesoscale feature at the base of the mixed layer is seen starting at 12:00 UTC on 1 February despite the continued strong surface forcing. The CO drifts over another weak stratification feature that extends up from the pycnocline as winds reduce to 3 m s^{-1} at 00:00 UTC on 2 February. The interplay between surface mixing and these frequent mesoscale features with a wide range of density gradient strengths observed during the MOSAiC drift complicates a 1D view of wind-forced turbulent momentum transfer into the ocean. Analysis of these mesoscale features is beyond the scope of the present paper, and will be explored in subsequent publications.

Strong inertial-period motions in the ocean mixed layer are capable of generating internal inertial-period waves within the pycnocline after the mixing layer inertial currents contact the strongly salinity-stratified pycnocline. In the current component profiles (Figures 13a and 13b) this can be seen as slanted bands of enhanced current shear with inertial periods starting around 45 m depth after the 1 February wind event. These regions of enhanced shear are also shown as black slanting lines in Figure 13c. These inertial waves are an important source of shear that can induce mixing in the otherwise very quiescent and non-diffusive Arctic pycnocline.

6 Discussion and conclusions

We presented a detailed description of an observed, strong, mid-winter, central Arctic cyclone which passed over the MOSAiC observatory from 31 January to 1 February 2020, closely following the passage of a weaker cyclone. This cyclone produced air-ice-ocean changes, including leading to the development and passage of a strong quasi-axisymmetric low-level jet (LLJ) in the lower atmosphere, producing widespread sea ice deformation, and propagating momentum flux into the upper ocean. The comprehensive suite of MOSAiC instruments together provides unique observations of the coupled air-ice-ocean system during an evolving cyclone with unprecedented detail and spatial resolution.

The developing atmospheric LLJ, which eventually appears as an annulus of ~140 km radius around the low-pressure center, is the key atmospheric feature of this cyclone impacting the momentum transfer to the sea ice. A smaller jet core within this LLJ is identified in the cold sector of the ERA5 reanalyses between 00 and 12 UTC on 1 February, and is linked to observed faster ice motion as well as shearing and divergence of the sea ice. The stage of storm development and the spatial structure of the LLJ strongly impacted the timing and location of sea ice deformation. The elevated surface wind speeds ahead of the cyclone produced an increase in drift speed and resulted in ice shear. The developed LLJ behind the cold front produced strong deformation in the ice, with divergence ahead of the jet core and convergence behind. This produced opening and closing of leads, respectively. Local sea-ice trajectories are a function of distance to the storm track and the side of the track. The sudden change in wind and ice-drift direction and the rapid increase in sea-ice velocity with the arrival of the cold-sector LLJ and its core produced a jump in the air-ice and ice-ocean stresses. The local destabilization of the lower atmosphere behind the cold front contributed to the former, while the latter initiated an inertial oscillation in the sea ice and upper ocean. The observations also showed that the change in ice-drift direction occurred locally in the DN about 2 h prior to the change in wind direction with the cold front, suggesting that wind forcing of the ice behind the cold front propagated ahead of the front through the internal ice stress. Hence, wind forcing of ice acceleration may not always occur locally.

The initiation of the inertial oscillation in the ocean extended the impacts of the storm beyond the time taken for the atmospheric depression to fully cross the observatory. A second increase in sea ice strain rates 12 hours after the arrival of the LLJ occurred due to the differing timescales between the atmosphere and the coupled ice-ocean boundary layer during the inertial oscillation and the gradual change in the wind direction. The ice and near-surface ocean returned to following the wind after approximately 24 hours, while at depth, the effects of the inertial oscillation were visible for at least 3 days.

Because of the apparent importance of the LLJ and the LLJ core for air-ice interactions, it must be noted that there is some uncertainty in its spatial and temporal structure. Since it was only directly observed by the 1 February 06:00 UTC sounding, and temporally and spatially spread by the ERA5 data assimilation, there could have been other LLJ cores or this core could have been present before 1 February 00:00 UTC. However, no atmospheric or ice observations suggest this to be the case. Furthermore, the structure and strength of the LLJ in the warm sector is also not well observed, as the 31 January 18:00 UTC sounding only captures the inner edge of the LLJ annulus at a time when the axisymmetric characteristic has not yet developed (Figure 3a). Hence, to describe the LLJ structure we use ERA5 to fill time and space between observations. Finally, LLJs have not been a part of the classical conceptual models of Arctic cyclones (e.g., Aizawa & Tanaka, 2016), likely due to these studies relying on reanalyses with a resolution incapable of resolving this mesoscale feature. More recent Arctic cyclone structure studies using ERA5 (e.g., Vessey et al., 2022), have mentioned the presence of strong low-level winds in the warm sector, however.

The breadth of observation types available through the MOSAiC observatory provides opportunity for numerical model evaluation and development, enabling examination of multi-scale, strongly coupled processes. While numerous case studies of cyclones exist, most focus on the summer and the marginal ice zone. Few observations are available for the central Arctic in full pack ice during mid-winter. We have identified key processes for the transfer of energy from atmosphere to sea ice to the upper ocean. A companion study will examine the representation of these processes in modern coupled air-ice-ocean numerical weather forecast models.

Acknowledgments

DW, OP, AS, and JKH were funded by the US Department of Energy (DoE), under grant DE-SC0021342. The participation of TS was funded through the National Science Foundation (NSF) OPP1723400. Atmospheric measurements and data processing were supported by NSF grant

OPP1724551 and the DoE Atmospheric Radiation Measurement Program. The deployment of GPS ice drifters and coordination within the MOSAiC DN was funded by NSF 1722729. OP also received support from the Office of Naval Research grant ONR 1564162 during the preparation of this manuscript.

We acknowledge the group effort required for the success of the MOSAiC expedition (Nixdorf et al., 2021).We additionally thank the MOSAiC distributed network team for additional GPS ice drift data and coordination of the L-sites and buoy deployments; the MOSAiC atmosphere team for supporting data collection during the MOSAiC field campaign, running instruments in the CO and maintaining the ASFS at L-sites; and the MOSAiC sea ice and snow team on MOSAiC Leg 2, in particular Polona Itkin, for supporting the ice radar data collection. The authors do not perceive any conflicts of interest.

Open Research

Atmospheric and ice drift data used in this paper are archived at the Arctic Data Center (Sea ice buoys: Bliss et al., 2022; atmospheric data: Cox et al., (2023a-d) and in the Alfred Wegner Institute PANGAEA archive (Maturilli et al., 2022). Atmospheric Ka-band radar is archived at the Department of Energy Atmospheric Radiation Measurement User Facility (Bharadwaj et al., 2019; Hardin et al., 2019). Ice radar data is archived in the Alfred Wegner Institute PANGAEA archive (Krumpen et al., 2021a). Data from the Autonomous Ocean Flux Buoy is archived at the Arctic Data Center (Stanton & Shaw, 2023). Code supporting the data analysis and visualization is archived at Zenodo (https://doi.org/10.5281/zenodo.10698905).

References

Aizawa, T., & Tanaka, H. L. (2016). Axisymmetric structure of the long lasting summer Arctic cyclones. *Polar Science*, *10*(3), 192–198. https://doi.org/10.1016/j.polar.2016.02.002

Andreas, E. L., Horst, T. W., Grachev, A. a., Persson, P. O. G., Fairall, C. W., Guest, P. S., & Jordan, R. E. (2010). Parametrizing turbulent exchange over summer sea ice and the marginal ice zone. *Quarterly Journal of the Royal Meteorological Society*, *136*(March), 927–943. https://doi.org/10.1002/qj.618

Andreas, E. L., Persson, P. O. G., Grachev, A. a., Jordan, R. E., Horst, T. W., Guest, P. S., & Fairall, C. W. (2010). Parameterizing Turbulent Exchange over Sea Ice in Winter. *Journal of Hydrometeorology*, *11*(1), 87–104. https://doi.org/10.1175/2009JHM1102.1

Aue, L., Vihma, T., Uotila, P., & Rinke, A. (2022). New Insights Into Cyclone Impacts on Sea Ice in the Atlantic Sector of the Arctic Ocean in Winter. *Geophysical Research Letters*, *49*(22). https://doi.org/10.1029/2022GL100051

Bharadwaj, N., Hardin, J., Isom, B., Johnson, K., Lindenmaier, I., Matthews, A., Nelson, D., Feng, Y.-C., Deng, M., Rocque, M., Castro, V., & Giangrande, T. (2019). *Ka-Band Scanning ARM Cloud Radar (KASACRCFR). 2020-01-29 to 2020-02-04, ARM Mobile Facility (MOS) MOSAIC (Drifting Obs—Study of Arctic Climate); AMF2 (M1)* [dataset]. Atmospheric Radiation Measurement (ARM) user facility. http://dx.doi.org/10.5439/1615726

Bliss, A. C., Hutchings, J. K., Anderson, P., Anhaus, P., Belter, H. J., Berge, J., Bessonov, V., Cheng, B., Cole, S., Costa, D., Cottier, F., Cox, C. J., de la Torre, R., Divine, D., Emzivat, G., Fang, Y. C., Fons, S., Gallagher, M., Geoffrey, M., … Zuo, G. (2022). *Sea ice drift tracks from the Distributed Network of autonomous buoys deployed during the Multidisciplinary drifting Observatory for the Study of Arctic Climate (MOSAiC) expedition 2019-2021*. Arctic Data Center. doi:10.18739/A2KP7TS83

Bliss, A. C., Hutchings, J. K., & Watkins, D. M. (2023). Sea ice drift tracks from autonomous buoys in the MOSAiC Distributed Network. *Scientific Data*, *10*(403), 1–10. https://doi.org/10.1038/s41597-023-02311-y

Bouillon, S., & Rampal, P. (2015). On producing sea ice deformation data sets from SAR-derived sea ice motion. *The Cryosphere*, *9*(2), 663–673. https://doi.org/10.5194/tc-9-663-2015

Brenner, S., Thomson, J., Rainville, L., Crews, L., & Lee, C. M. (2023). Wind-Driven Motions of the Ocean Surface Mixed Layer in the Western Arctic. *Journal of Physical Oceanography*, *53*(7), 1787–1804. https://doi.org/10.1175/JPO-D-22-0112.1

Brümmer, B. (2003). A Fram Strait cyclone: Properties and impact on ice drift as measured by aircraft and buoys. *Journal of Geophysical Research*, *108*(D7), 4217. https://doi.org/10.1029/2002JD002638

Brümmer, B., & Hoeber, H. (1999). A mesoscale cyclone over the Fram Strait and its effects on sea ice. *Journal of Geophysical Research: Atmospheres*, *104*(D16), 19085–19098. https://doi.org/10.1029/1999JD900259

Brümmer, B., Schröder, D., Müller, G., Spreen, G., Jahnke-Bornemann, A., & Launiainen, J. (2008). Impact of a Fram Strait cyclone on ice edge, drift, divergence, and concentration: Possibilities and limits of an observational analysis. *Journal of Geophysical Research: Oceans*, *113*(12), 1–15. https://doi.org/10.1029/2007JC004149

Clancy, R., Bitz, C. M., Blanchard-Wrigglesworth, E., McGraw, M. C., & Cavallo, S. M. (2022). A cyclone-centered perspective on the drivers of asymmetric patterns in the atmosphere and sea ice during Arctic cyclones. *Journal of Climate*, 1–47. https://doi.org/10.1175/JCLI-D-21-0093.1

Cox, C., Gallagher, M., Shupe, M., Blomquist, B., Persson, O., Grachev, A., Riihimaki, L. D., Kutchenreiter, M., Morris, V., Solomon, A., Brooks, I., Costa, D., Gottas, D., Hutchings, J. K., Osborn, J., Morris, S. M., Preusser, A., & Uttal, T. (2023). *Met City meteorological and surface flux measurements (Level 3 Final), Multidisciplinary Drifting Observatory* *for the Study of Arctic Climate (MOSAiC), central Arctic, October 2019—September 2020* [dataset]. Arctic Data Center. https://doi.org/10.18739/A2PV6B83F

Cox, C., Gallagher, M., Shupe, M., Persson, O., Grachev, A., Solomon, A., Ayers, T., Costa, D., Hutchings, J. K., Leach, J., Morris, S. M., Osborn, J., Pezoa, S., & Uttal, T. (2023a). *Atmospheric Surface Flux Station #30 measurements (Level 3 Final), Multidisciplinary Drifting Observatory for the Study of Arctic Climate (MOSAiC), central Arctic, October 2019—September 2020* [dataset]. Arctic Data Center. https://doi.org/10.18739/A2FF3M18K

Cox, C., Gallagher, M., Shupe, M., Persson, O., Grachev, A., Solomon, A., Ayers, T., Costa, D., Hutchings, J. K., Leach, J., Morris, S. M., Osborn, J., Pezoa, S., & Uttal, T. (2023b). *Atmospheric Surface Flux Station #40 measurements (Level 3 Final), Multidisciplinary Drifting Observatory for the Study of Arctic Climate (MOSAiC), central Arctic, October 2019—September 2020* [dataset]. Arctic Data Center. https://doi.org/10.18739/A2FF3M18K

Cox, C., Gallagher, M., Shupe, M., Persson, O., Grachev, A., Solomon, A., Ayers, T., Costa, D., Hutchings, J. K., Leach, J., Morris, S. M., Osborn, J., Pezoa, S., & Uttal, T. (2023c). *Atmospheric Surface Flux Station #50 measurements (Level 3 Final), Multidisciplinary Drifting Observatory for the Study of Arctic Climate (MOSAiC), central Arctic, October 2019—September 2020* [dataset]. Arctic Data Center. https://doi.org/10.18739/A2XD0R00S

Cox, C. J., Gallagher, M. R., Shupe, M. D., Persson, P. O. G., Solomon, A., Fairall, C. W., Ayers, T., Blomquist, B., Brooks, I. M., Costa, D., Grachev, A., Gottas, D., Hutchings, J. K., Kutchenreiter, M., Leach, J., Morris, S. M., Morris, V., Osborn, J., Pezoa, S., … Uttal, T. (2023). Continuous observations of the surface energy budget and meteorology over the Arctic sea ice during MOSAiC. *Scientific Data*, *10*(1), 519. https://doi.org/10.1038/s41597-023-02415-5

Deser, C., Tomas, R. A., & Sun, L. (2015). The role of ocean-atmosphere coupling in the zonal-mean atmospheric response to Arctic sea ice loss. *Journal of Climate*, *28*(6), 2168–2186. https://doi.org/10.1175/JCLI-D-14-00325.1

Etling, D., & Brown, R. A. (1993). Roll vortices in the planetary boundary layer: A review. *Boundary-Layer Meteorology*, *65*(3), 215–248. https://doi.org/10.1007/BF00705527

Fearon, M. G., Doyle, J. D., Ryglicki, D. R., Finocchio, P. M., & Sprenger, M. (2021). The Role of Cyclones in Moisture Transport into the Arctic. *Geophysical Research Letters*, *48*(4), e2020GL090353. https://doi.org/10.1029/2020GL090353

Fer, I., Baumann, T. M., Koenig, Z., Muilwijk, M., & Tippenhauer, S. (2022). Upper-Ocean Turbulence Structure and Ocean-Ice Drag Coefficient Estimates Using an Ascending Microstructure Profiler During the MOSAiC Drift. *Journal of Geophysical Research: Oceans*, *127*(9). https://doi.org/10.1029/2022JC018751

Gallaher, S. G., Stanton, T. P., Shaw, W. J., Cole, S. T., Toole, J. M., Wilkinson, J. P., Maksym, T., & Hwang, B. (2016). Evolution of a Canada Basin ice-ocean boundary layer and mixed layer across a developing thermodynamically forced marginal ice zone. *Journal of Geophysical Research: Oceans*, *121*(8), 6223–6250. https://doi.org/10.1002/2016JC011778

Gimbert, F., Marsan, D., Weiss, J., Jourdain, N. C., & Barnier, B. (2012). Sea ice inertial oscillations in the Arctic Basin. *The Cryosphere*, *6*(5), 1187–1201. https://doi.org/10.5194/tc-6-1187-2012

Grachev, A. A., Andreas, E. L., Fairall, C. W., Guest, P. S., & Persson, P. O. G. (2007). SHEBA flux–profile relationships in the stable atmospheric boundary layer. *Boundary-Layer Meteorology*, *124*(3), 315–333. https://doi.org/10.1007/s10546-007-9177-6

Graham, R. M., Cohen, L., Ritzhaupt, N., Segger, B., Graversen, R. G., Rinke, A., Walden, V. P., Granskog, M. A., & Hudson, S. R. (2019). Evaluation of six atmospheric reanalyses over Arctic sea ice from winter to early summer. *Journal of Climate*, *32*(14), 4121–4143. https://doi.org/10.1175/JCLI-D-18-0643.1

Graham, R. M., Hudson, S. R., & Maturilli, M. (2019). Improved performance of ERA5 in Arctic gateway relative to four global atmospheric reanalyses. *Geophysical Research Letters*, *46*(11), 6138–6147. https://doi.org/10.1029/2019GL082781

Haapala, J., Lönnroth, N., & Stössel, A. (2005). A numerical study of open water formation in sea ice. *Journal of Geophysical Research*, *110*(C9), C09011. https://doi.org/10.1029/2003JC002200

Haller, M., Brümmer, B., & Müller, G. (2014). Atmosphere–ice forcing in the transpolar drift stream: Results from the DAMOCLES ice-buoy campaigns 2007–2009. *The Cryosphere*, *8*(1), 275–288. https://doi.org/10.5194/tc-8-275-2014

Hardin, J., Hunzinger, A., Schuman, E., Matthews, A., Bharadwaj, N., Varble, A., Johnson, K., Giangrande, S., Feng, Y.-C., & Lindenmaier, I. (2019). *Ka ARM Zenith Radar (KAZRCFRGEQC). 2020-01-29 to 2020-02-05, ARM Mobile Facility (MOS) MOSAIC (Drifting Obs—Study of Arctic Climate); AMF2 (M1)*. Atmospheric Radiation Measurement (ARM) user facility. https://doi.org/10.5439/1615726

Hersbach, H., Bell, B., Berrisford, P., Biavati, G., Horányi, A., Muñoz Sabater, J., Nicolas, J., Radu, C., Rozum, I., Schepers, D., Simmons, A., Soci, C., Dee, D., & Thépaut, J. (2023a). *ERA5 hourly data on pressure levels from 1940 to present.* [dataset]. Copernicus Climate Change Service (C3S) Climate Data Store (CDS). https://doi.org/10.24381/cds.bd0915c6

Hersbach, H., Bell, B., Berrisford, P., Biavati, G., Horányi, A., Muñoz Sabater, J., Nicolas, J., Radu, C., Rozum, I., Schepers, D., Simmons, A., Soci, C., Dee, D., & Thépaut, J. (2023b). *ERA5 hourly data on single levels from 1940 to present.* [dataset]. Copernicus Climate Change Service (C3S) Climate Data Store (CDS). https://doi.org/10.24381/cds.adbb2d47

Hersbach, H., Bell, B., Berrisford, P., Hirahara, S., Horányi, A., Nicolas, J., Peubey, C., Radu, R., Bonavita, M., Dee, D., Dragani, R., Flemming, J., Forbes, R., Geer, A., Hogan, R. J., Janisková, H. M., Keeley, S., Laloyaux, P., Cristina, P. L., & Thépaut, J. (2020). The ERA5 global reanalysis. *Quarterly Journal of the Royal Meteorological Society*, *June*, 1999–2049. https://doi.org/10.1002/qj.3803

Hessner, El Naggar, Von Appen, & Strass. (2019). On the Reliability of Surface Current Measurements by X-band Marine Radar. *Remote Sensing*, *11*(9), 1030. https://doi.org/10.3390/rs11091030

Hibler, W. D. (1979). A Dynamic Thermodynamic Sea Ice Model. *Journal of Physical Oceanography*, *9*(4), 815–846. https://doi.org/10.1175/1520-0485(1979)009<0815:ADTSIM>2.0.CO;2

Hunke, E. C., Lipscomb, W. H., Turner, A. K., Jeffery, N., & Elliott, S. (2015). *CICE : the Los Alamos Sea Ice Model Documentation and Software User's Manual* [Computer software].

Hunkins, K. (1967). Inertial oscillations of Fletcher's Ice Island (T-3). *Journal of Geophysical Research*, *72*(4), 1165–1174. https://doi.org/10.1029/JZ072i004p01165

Hutchings, J. K., Heil, P., Steer, A., & Hibler, W. D. (2012). Subsynoptic scale spatial variability of sea ice deformation in the western Weddell Sea during early summer. *Journal of Geophysical Research*, *117*(C1), C01002. https://doi.org/10.1029/2011JC006961

Hutchings, J. K., Roberts, A., Geiger, C. A., & Richter-Menge, J. (2018). Corrigendum: Spatial and temporal characterisation of sea-ice deformation. *Journal of Glaciology*, *64*(244), 343–346. https://doi.org/10.1017/jog.2018.11

Itkin, P., Spreen, G., Cheng, B., Doble, M., Girard-Ardhuin, F., Haapala, J., Hughes, N., Kaleschke, L., Nicolaus, M., & Wilkinson, J. (2017). Thin ice and storms: Sea ice deformation from buoy arrays deployed during N-ICE2015. *Journal of Geophysical Research: Oceans*, *122*(6), 4661–4674. https://doi.org/10.1002/2016JC012403

Kaimal, J. C., & Finnigan, J. J. (1994). *Atmospheric boundary layer flows: Their structure and measurement*. Oxford University Press. https://doi.org/10.1093/oso/9780195062397.001.0001

Kriegsmann, A., & Brümmer, B. (2014). Cyclone impact on sea ice in the central Arctic Ocean: A statistical study. *The Cryosphere*, *8*(1), 303–317. https://doi.org/10.5194/tc-8-303-2014

Krumpen, T., Birrien, F., Kauker, F., Rackow, T., von Albedyll, L., Angelopoulos, M., Belter, H. J., Bessonov, V., Damm, E., Dethloff, K., Haapala, J., Haas, C., Hendricks, S., Hoelemann, J., Hoppmann, M., Kaleschke, L., Karcher, M., Kolabutin, N., Lenz, J., … Watkins, D. M. (2020). The MOSAiC ice floe: Sediment-laden survivor from the Siberian shelf. *The Cryosphere*, *14*, 2173–2187. https://doi.org/10.5194/tc-2020-64

Krumpen, T., Haapala, J., Krocker, R., & Bartsch, A. (2021). *Ice radar raw data (sigma S6 ice radar) of RV POLARSTERN during cruise PS122/1*. PANGAEA / Alfred Wegener Institute, Helmholtz Centre for Polar and Marine Research, Bremerhaven. https://doi.org/10.1594/PANGAEA.929434

Krumpen, T., von Albedyll, L., Goessling, H. F., Hendricks, S., Juhls, B., Spreen, G., Willmes, S., Belter, H. J., Dethloff, K., Haas, C., Kaleschke, L., Katlein, C., Tian-Kunze, X., Ricker, R., Rostosky, P., Rückert, J., Singha, S., & Sokolova, J. (2021). MOSAiC drift expedition from October 2019 to July 2020: Sea ice conditions from space and comparison with previous years. *The Cryosphere*, *15*(8), 3897–3920. https://doi.org/10.5194/tc-15-3897-2021

Kwok, R., Spreen, G., & Pang, S. (2013). Arctic sea ice circulation and drift speed: Decadal trends and ocean currents. *Journal of Geophysical Research: Oceans*, *118*(5), 2408–2425. https://doi.org/10.1002/jgrc.20191

LeMone, M. A. (1973). The Structure and Dynamics of Horizontal Roll Vortices in the Planetary Boundary Layer. *Journal of the Atmospheric Sciences*, *30*, 1077–1091. https://doi.org/10.1175/1520-0469(1973)030<1077:TSADOH>2.0.CO;2

Leppäranta, M. (2007). *The drift of sea ice*. Springer Berlin Heidelberg. https://books.google.com/books?id=MMIXaOl1jxwC

Lindsay, R. W. (2002). Ice deformation near SHEBA. *Journal of Geophysical Research*, *107*(C10), 8042. https://doi.org/10.1029/2000JC000445

Lindsay, R. W., & Stern, H. L. (2003). The RADARSAT Geophysical Processor System: Quality of sea ice trajectory and deformation estimates. *Journal of Atmospheric and Oceanic Technology*, *20*(9), 1333–1347. https://doi.org/10.1175/1520-0426(2003)020<1333:TRGPSQ>2.0.CO;2

Long, M., Zhang, L., Hu, S., & Qian, S. (2021). Multi-Aspect Assessment of CMIP6 Models for Arctic Sea Ice Simulation. *Journal of Climate*, *34*(4), 1515–1529. https://doi.org/10.1175/JCLI-D-20-0522.1

López-García, V., Neely, R. R., Dahlke, S., & Brooks, I. M. (2022). Low-level jets over the Arctic Ocean during MOSAiC. *Elementa: Science of the Anthropocene*, *10*(1), 00063. https://doi.org/10.1525/elementa.2022.00063

Lüpkes, C., & Gryanik, V. M. (2015). A stability-dependent parametrization of transfer coefficients formomentum and heat over polar sea ice to be used in climate models. *Journal of Geophysical Research: Atmospheres*, *120*(2), 552–581. https://doi.org/10.1002/2014JD022418

Lüpkes, C., Gryanik, V. M., Witha, B., Gryschka, M., Rassch, S., & Gollnik, T. (2008). Modeling convection over arctic leads with LES and a non-eddy-resolving microscale model. *Journal of Geophysical Research: Oceans*, *113*(9), 1–17. https://doi.org/10.1029/2007JC004099

Martini, K. I., Simmons, H. L., Stoudt, C. A., & Hutchings, J. K. (2014). Near-inertial internal waves and sea ice in the Beaufort Sea. *Journal of Physical Oceanography*, *44*(8), 2212–2234. https://doi.org/10.1175/JPO-D-13-0160.1

Maturilli, M., Sommer, M., Holdridge, D. J., Dahlke, S., Graeser, J., Sommerfeld, A., Jaiser, R., Deckelmann, H., & Schulz, A. (2022). *MOSAiC radiosonde data (level 3)*. PANGAEA. https://doi.org/10.1594/PANGAEA.943870

Maykut, G. A. (1982). Large-scale heat exchange and ice production in the central Arctic. *Journal of Geophysical Research: Oceans*, *87*(C10), 7971–7984. https://doi.org/10.1029/JC087iC10p07971

McNutt, S. L., & Overland, J. E. (2003). Spatial hierarchy in Arctic sea ice dynamics. *Tellus A: Dynamic Meteorology and Oceanography*, *55*(2), 181–191. https://doi.org/10.3402/tellusa.v55i2.12088

McPhee, M. G. (2002). Turbulent stress at the ice/ocean interface and bottom surface hydraulic roughness during the SHEBA drift. *Journal of Geophysical Research*, *107*(C10), 8037. https://doi.org/10.1029/2000JC000633

McPhee, M. G. (2008). *Air-Ice-Ocean Interaction: Turbulent Ocean Boundary Layer Exchange Processes* (1st ed.). Springer. https://doi.org/10.1007/978-0-387-78335-2

McPhee, M. G., & Kantha, L. H. (1989). Generation of internal waves by sea ice. *Journal of Geophysical Research*, *94*(C3), 3287. https://doi.org/10.1029/JC094iC03p03287

Meyer, A., Fer, I., Sundfjord, A., & Peterson, A. K. (2017). Mixing rates and vertical heat fluxes north of Svalbard from Arctic winter to spring. *Journal of Geophysical Research: Oceans*, *122*(6), 4569–4586. https://doi.org/10.1002/2016JC012441

Meyer, A., Sundfjord, A., Fer, I., Provost, C., Villacieros Robineau, N., Koenig, Z., Onarheim, I. H., Smedsrud, L. H., Duarte, P., Dodd, P. A., Graham, R. M., Schmidtko, S., & Kauko, H. M. (2017). Winter to summer oceanographic observations in the Arctic Ocean north of Svalbard. *Journal of Geophysical Research: Oceans*, *122*(8), 6218–6237. https://doi.org/10.1002/2016JC012391

Nansen, F. (1902). *The Norwegian North polar expedition, 1893-1896: Scientific Results*. London ; New York : Longmans, Green and Co. ; Christiania : J. Dybwad, 1900-1906.

Nicolaus, M., Perovich, D. K., Spreen, G., Granskog, M. A., von Albedyll, L., Angelopoulos, M., Anhaus, P., Arndt, S., Belter, H. J., Bessonov, V., Birnbaum, G., Brauchle, J., Calmer, R., Cardellach, E., Cheng, B., Clemens-Sewall, D., Dadic, R., Damm, E., de Boer, G., … Wendisch, M. (2022). Overview of the MOSAiC expedition: Snow and sea ice. *Elementa: Science of the Anthropocene*, *10*(1). https://doi.org/10.1525/elementa.2021.000046

Nixdorf, U., Dethloff, K., Rex, M., Shupe, M., Sommerfeld, A., Perovich, D. K., Nicolaus, M., Heuzé, C., Rabe, B., Loose, B., Damm, E., Gradinger, R., Fong, A., Maslowski, W., Rinke, A., Kwok, R., Spreen, G., Wendisch, M., Herber, A., … Boetius, A. (2021). *MOSAiC extended acknowledgement*. Zenodo. https://doi.org/10.5281/zenodo.5179738

Oikkonen, A., Haapala, J., Lensu, M., Karvonen, J., & Itkin, P. (2017). Small-scale sea ice deformation during N-ICE2015: From compact pack ice to marginal ice zone. *Journal of Geophysical Research: Oceans*, *122*, 5105–5120.

Overland, J. E. (1985). Atmospheric boundary layer structure and drag coefficients over sea ice. *Journal of Geophysical Research: Oceans*, *90*(C5), 9029–9049. https://doi.org/10.1029/JC090iC05p09029

Overland, J. E., & Pease, C. H. (1982). Cyclone climatology of the Bering Sea and its relation to sea ice extent. *Monthly Weather Review*, *110*, 5–13.

Peng, S., Yang, Q., Shupe, M. D., Xi, X., Han, B., Chen, D., Dahlke, S., & Liu, C. (2023). The characteristics of atmospheric boundary layer height over the Arctic Ocean during MOSAiC. *Atmospheric Chemistry and Physics*, *23*(15), 8683–8703. https://doi.org/10.5194/acp-23-8683-2023

Persson, O., Cox, C. J., Gallagher, M. R., Shupe, M. D., Hutchings, J. K., Watkins, D. M., & Perovich, D. K. (2023). *Arctic Cyclone Cloud and Boundary-Layer Features Producing Thermodynamic and Dynamic Impacts on Arctic Sea Ice During MOSAiC. EGU23-17554*. https://doi.org/10.5194/egusphere-egu23-17554

Persson, P. O. G. (2002). Measurements near the Atmospheric Surface Flux Group tower at SHEBA: Near-surface conditions and surface energy budget. *Journal of Geophysical Research*, *107*(C10), 1–35. https://doi.org/10.1029/2000JC000705

Persson, P. O. G. (2012). Onset and end of the summer melt season over sea ice: Thermal structure and surface energy perspective from SHEBA. *Climate Dynamics*, *39*, 1349–1371. https://doi.org/10.1007/s00382-011-1196-9

Persson, P. O. G., Shupe, M. D., Perovich, D., & Solomon, A. (2017). Linking atmospheric synoptic transport, cloud phase, surface energy fluxes, and sea-ice growth: Observations of midwinter SHEBA conditions. *Climate Dynamics*, *49*(4), 1341–1364. https://doi.org/10.1007/s00382-016-3383-1

Petty, A. A., Hutchings, J. K., Richter-Menge, J. A., & Tschudi, M. A. (2016). Sea ice circulation around the Beaufort Gyre: The changing role of wind forcing and the sea ice state. *Journal of Geophysical Research*, 19.

Pinto, J. O., Alam, A., Maslanik, J. A., Curry, J. A., & Stone, R. S. (2003). Surface characteristics and atmospheric footprint of springtime Arctic leads at SHEBA. *Journal of Geophysical Research: Oceans*, *108*(C4), 8051. https://doi.org/10.1029/2000JC000473

Rabe, B., Cox, C. C., Fang, Y.-C., Goessling, H., Granskog, M. A., Hoppmann, M., Hutchings, J. K., Krumpen, T., Kuznetsov, I., Lei, R., Li, T., Maslowski, W., Nicolaus, M., Perovich, D., Persson, O., Regnery, J., Rigor, I., Shupe, M. D., Sokolov, V., … Zuo, G. (2024). MOSAiC Distributed Network: Observing the coupled Arctic system with multidisciplinary, coordinated platforms. *Elementa: Science of the Anthropocene*, *Accepted*.

Rabe, B., Heuzé, C., Regnery, J., Aksenov, Y., Allerholt, J., Athanase, M., Davies, A., Damm, E., Dethloff, K., Divine, D. V., Doglioni, F., & Craw, L. (2022). Overview of the MOSAiC expedition: Physical oceanography. *Elementa: Science of the Anthropocene*, *10*, 1–31. https://doi.org/10.1525/elementa.2021.00062

Rae, J. G. L., Todd, A. D., Blockley, E. W., & Ridley, J. K. (2017). How much should we believe correlations between Arctic cyclones and sea ice extent? *The Cryosphere*, *11*(6), 3023–3034. https://doi.org/10.5194/tc-11-3023-2017

Rainville, L., & Woodgate, R. A. (2009). Observations of internal wave generation in the seasonally ice-free Arctic. *Geophysical Research Letters*, *36*(23), L23604. https://doi.org/10.1029/2009GL041291

Richter-Menge, J. A., Perovich, D. K., & Pegau, W. S. (2001). Summer ice dynamics during SHEBA and its effect on the ocean heat content. *Annals of Glaciology*, *33*, 201–206. https://doi.org/10.3189/172756401781818176

Rinke, A., Cassano, J. J., Cassano, E. N., Jaiser, R., & Handorf, D. (2021). Meteorological conditions during the MOSAiC expedition. *Elementa: Science of the Anthropocene*, *9*(1), 1–17. https://doi.org/10.1525/elementa.2021.00023

Roberts, A., Craig, A., Maslowski, W., Osinski, R., DuVIVIER, A., Hughes, M., Nijssen, B., Cassano, J., & Brunke, M. (2015). Simulating transient ice–ocean Ekman transport in the Regional Arctic System Model and Community Earth System Model. *Annals of Glaciology*, *56*(69), 211–228. https://doi.org/10.3189/2015AoG69A760

Ruffieux, D., Persson, P. O. G., Fairall, C. W., & Wolfe, D. E. (1995). Ice pack and lead surface energy budgets during LEADEX 1992. *Journal of Geophysical Research: Oceans*, *100*(C3), 4593–4612. https://doi.org/10.1029/94JC02485

Sandven, S., Spreen, G., Heygster, G., Girard-Ardhuin, F., Farrell, S. L., Dierking, W., & Allard, R. A. (2023). Sea Ice Remote Sensing—Recent Developments in Methods and Climate Data Sets. *Surveys in Geophysics*. https://doi.org/10.1007/s10712-023-09781-0

Schweiger, A. J., & Zhang, J. (2015). Accuracy of short-term sea ice drift forecasts using a coupled ice-ocean model. *Journal of Geophysical Research: Oceans*, 15.

Shaw, W. J., Stanton, T. P., McPhee, M. G., Morison, J. H., & Martinson, D. G. (2009). Role of the upper ocean in the energy budget of Arctic sea ice during SHEBA. *Journal of Geophysical Research*, *114*(C6), C06012. https://doi.org/10.1029/2008JC004991

Shupe, M. D., & Rex, M. (2022). A year in the changing Arctic sea ice. *Oceanography*, *35*(3–4), 224–225.

Shupe, M. D., Rex, M., Blomquist, B., Persson, P. O. G., Schmale, J., Uttal, T., Buck, C., Boyer, M., Hofer, J., Hamilton, J., Posman, K., Powers, H., Pratt, K. A., Preußer, A., Rabe, B., & Rinke, A. (2022). Overview of the MOSAiC expedition-Atmosphere. *Elementa: Science of the Anthropocene*, *10*(1), 1–54. https://doi.org/10.1525/elementa.2021.00060

Shupe, M. D., Rex, M., Dethloff, K., Damm, E., Fong, A. A., Gradinger, R., Heuzé, C., Loose, B., Makarov, A., Maslowski, W., Nicolaus, M., Perovich, D., Rabe, B., Rinke, A., Sokolov, V., & Sommerfeld, A. (2020). *Arctic Report Card 2020: The MOSAiC Expedition: A Year Drifting with the Arctic Sea Ice*. https://doi.org/10.25923/9G3V-XH92

Stanton, T. P., & Shaw, W. J. (2023). *Observations from Autonomous Ocean Flux Buoy 46 deployed at site CO during the MOSAiC transpolar drift, Arctic Basin, 2019-2020* [dataset]. Arctic Data Center. https://doi.org/10.18739

Stanton, T. P., Shaw, W. J., & Hutchings, J. K. (2012). Observational study of relationships between incoming radiation, open water fraction, and ocean-to-ice heat flux in the Transpolar Drift: 2002-2010: OCEAN/ICE FLUXES IN THE ARCTIC. *Journal of Geophysical Research: Oceans*, *117*(C7), n/a-n/a. https://doi.org/10.1029/2011JC007871

Taylor, K. E., Stouffer, R. J., & Meehl, G. a. (2012). An overview of CMIP5 and the experiment design. *Bulletin of the American Meteorological Society*, *93*(4), 485–498. https://doi.org/10.1175/BAMS-D-11-00094.1

Taylor, P. C., Hegyi, B. M., Boeke, R. C., & Boisvert, L. N. (2018). On the increasing importance of air-sea exchanges in a thawing Arctic: A review. *Atmosphere*, *9*(2), 1–39. https://doi.org/10.3390/atmos9020041

Thorndike, A. S. (1986). Diffusion of sea ice. *Journal of Geophysical Research*, *91*(C6), 7691. https://doi.org/10.1029/JC091iC06p07691

Toole, J. M., Timmermans, M. -L., Perovich, D. K., Krishfield, R. A., Proshutinsky, A., & Richter-Menge, J. A. (2010). Influences of the ocean surface mixed layer and thermohaline stratification on Arctic Sea ice in the central Canada Basin. *Journal of*

Geophysical Research: Oceans, *115*(C10), 2009JC005660. https://doi.org/10.1029/2009JC005660

Uttal, T., Curry, J. A., McPhee, M. G., Perovich, D. K., Moritz, R. E., Maslanik, J. A., Guest, P. S., Stern, H. L., Moore, J. A., Turenne, R., Heiberg, A., Serreze, M. C., Wylie, D. P., Persson, O. G., Paulson, C. A., Halle, C., Marison, J. H., Wheeler, P. A., Makshtas, A., … Grenfeld, T. C. (2002). Surface heat budget of the arctic ocean. *Bulletin of the American Meteorological Society*, *83*(2), 255–275. https://doi.org/10.1175/1520-0477(2002)083<0255:SHBOTA>2.3.CO;2

Vessey, A. F., Hodges, K. I., Shaffrey, L. C., & Day, J. J. (2020). An inter-comparison of Arctic synoptic scale storms between four global reanalysis datasets. *Climate Dynamics*, 2777–2795.

Vessey, A. F., Hodges, K. I., Shaffrey, L. C., & Day, J. J. (2022). The composite development and structure of intense synoptic-scale Arctic cyclones. *Weather and Climate Dynamics*, *3*(3), 1097–1112. https://doi.org/10.5194/wcd-3-1097-2022

von Albedyll, L., Hendricks, S., Grodofzig, R., Krumpen, T., Arndt, S., Belter, H. J., Birnbaum, G., Cheng, B., Hoppmann, M., Hutchings, J., Itkin, P., Lei, R., Nicolaus, M., Ricker, R., Rohde, J., Suhrhoff, M., Timofeeva, A., Watkins, D., Webster, M., & Haas, C. (2022). Thermodynamic and dynamic contributions to seasonal Arctic sea ice thickness distributions from airborne observations. *Elementa: Science of the Anthropocene*, *10*(1), 00074. https://doi.org/10.1525/elementa.2021.00074

Wang, C., Graham, R. M., Wang, K., Gerland, S., & Granskog, M. A. (2019). Comparison of ERA5 and ERA-Interim near-surface air temperature, snowfall and precipitation over Arctic sea ice: Effects on sea ice thermodynamics and evolution. *The Cryosphere*, *13*(6), 1661–1679. https://doi.org/10.5194/tc-13-1661-2019

Wang, X., Chen, R., Li, C., Chen, Z., Hui, F., & Cheng, X. (2022). An Intercomparison of Satellite Derived Arctic Sea Ice Motion Products. *Remote Sensing*, *14*(5), 1261. https://doi.org/10.3390/rs14051261

Watkins, D. M., Bliss, A. C., Hutchings, J. K., & Wilhelmus, M. M. (2023). Evidence of Abrupt Transitions Between Sea Ice Dynamical Regimes in the East Greenland Marginal Ice Zone. *Geophysical Research Letters*, *50*(e2023GL103558), 1–10.

Webster, M. A., Parker, C., Boisvert, L., & Kwok, R. (2019). The role of cyclone activity in snow accumulation on Arctic sea ice. *Nature Communications*, *10*(1), 5285. https://doi.org/10.1038/s41467-019-13299-8

Womack, A., Vichi, M., Alberello, A., & Toffoli, A. (2022). Atmospheric drivers of a winter-to-spring Lagrangian sea-ice drift in the Eastern Antarctic marginal ice zone. *Journal of Glaciology*. https://doi.org/10.1017/jog.2022.14

Yang, J. (2004). Storm-driven mixing and potential impact on the Arctic Ocean. *Journal of Geophysical Research*, *109*(C4), C04008. https://doi.org/10.1029/2001JC001248

Yu, Y., Xiao, W., Zhang, Z., Cheng, X., Hui, F., & Zhao, J. (2021). Evaluation of 2-m Air Temperature and Surface Temperature from ERA5 and ERA-I Using Buoy Observations in the Arctic during 2010–2020. *Remote Sensing*, *13*(14), 2813. https://doi.org/10.3390/rs13142813

Yuan, D., Hao, Z., You, J., Zhang, P., Yin, B., Li, Q., & Xu, Z. (2022). Enhancing Sea Ice Inertial Oscillations in the Arctic Ocean between 1979 and 2019. *Water*, *15*(1), 152. https://doi.org/10.3390/w15010152